

Report

R-20-05

June 2021



Rock mass effective properties from a DFN approach

Phase 1 – Elastic properties

Caroline Darcel
Romain Le Goc
Diane Doolaeghe
Rima Ghazal
Philippe Davy

SVENSK KÄRNBRÄNSLEHANTERING AB

SWEDISH NUCLEAR FUEL
AND WASTE MANAGEMENT CO

Box 3091, SE-169 03 Solna
Phone +46 8 459 84 00
skb.se

SVENSK KÄRNBRÄNSLEHANTERING

ISSN 1402-3091

SKB R-20-05

ID 1907393

June 2021

Rock mass effective properties from a DFN approach

Phase 1 – Elastic properties

Caroline Darcel, Romain Le Goc, Diane Doolaeghe, Rima Ghazal
Itasca Consultants s.a.s

Philippe Davy, CNRS, Géosciences Rennes

Keywords: Discrete Fracture Network (DFN), Rock mechanics, Rock mass, Elastic properties.

This report concerns a study which was conducted for Svensk Kärnbränslehantering AB (SKB). The conclusions and viewpoints presented in the report are those of the authors. SKB may draw modified conclusions, based on additional literature sources and/or expert opinions.

This report is published on www.skb.se

© 2021 Svensk Kärnbränslehantering AB

Executive summary

This report summarizes the work completed over the period from March 2016 to June 2019, for the development of a methodology to derive rock mass effective elastic properties from a Discrete Fracture Network modelling approach. The objective is to significantly reduce the rock mass mechanical modelling uncertainties, which are above all related to the geometrical and mechanical properties of the fracture network, especially relative to scaling and anisotropy issues. It is also to better address, in the numerical models, the issues raised by the complex nature of the rock fractured system (e.g. discrete/continuous representation). The guideline for the project is to understand the physical role played by the fractures on the rock mass mechanical response and use of it to develop the modelling methodology. The rock mass is viewed as an assembly of discrete fractures embedded in a rock matrix with uniform elastic properties.

The first phase of the development is the determination of equivalent effective elastic properties (simply Young's modulus and Poisson's ratio or compliance tensor in the general case) of any rock mass specimen, at a Discrete Fracture Network (DFN) scale. The theoretical developments made were published in the Journal of Geophysical Research (Davy et al. 2018) during the project. They rely on the accumulation, at the rock mass scale, of the shear and normal displacements of each individual fracture of the DFN population.

At a single fracture scale, relations are first established between the remote loading conditions, the fracture displacement and the resulting deformation at the rock mass scale. The fracture mechanical model is based on the Coulomb slip constitutive model, where the fracture normal displacement is proportional to the normal stiffness k_n , and the fracture shear displacement is proportional to the shear stiffness k_s , below a critical shear stress and in a slipping state when the threshold is reached. Both the normal and shear stiffnesses may be dependent on the fracture size or orientation, or on the stress state.

The first key point is relative to the stress partitioning between the resistances of a fracture plane and of the rock matrix around the fracture. The relative contribution of both depends on the combination between the fracture size, the surrounding rock modulus and the shear stiffness of the fracture k_s . A key length scale is defined, called the stiffness size l_s , from the ratio of the intact rock modulus E_m to the fracture shear stiffness k_s . It is demonstrated that fractures which are much larger than l_s are dominated by a fracture shear stiffness regime, while fractures smaller than l_s are dominated by a "matrix stiffness" (noted k_m) regime, where k_m is proportional to E_m/l and where l is the fracture size.

A relation is established to sum the contributions of each individual fracture to the rock mass scale deformation. An effective theory is applied to account for the interactions between fractures when the DFN densities are significant. All the theoretical developments are checked with numerical simulations performed with the 3DEC software. At the end of this development phase, the defined relations allow deriving the effective elastic properties for any rock mass containing any DFN network. The methodology is applied to several cases, to emphasize the capacity of the approach to predict and to relate the scaling and anisotropy of the rock mass properties to the scaling and anisotropy of the DFN models.

In addition to the rock mass scale study and determination of effective elastic properties, the spatial distribution of stresses – the stress fluctuations below the rock mass scale at which effective properties are evaluated – relative to the spatial distribution of the fractures in the rock mass, is analysed. Several tensorial and scalar indicators are used and compared. These analyses are part of a preliminary methodology development phase and will be further continued towards predicting the intensity of stress fluctuations and the strength of the rock mass and optimizing the representation of the rock mass, as a combination between effective properties and discrete fractures.

Sammanfattning

Denna rapport summerar det arbete som utförts under perioden mars 2016 till juni 2019, för utveckling av metodiken att beräkna bergmassans effektiva elastiska egenskaper med ett angreppssätt som bygger på diskreta spricknätverk (DFN). Målet är att signifikant reducera osäkerheten i bergmekanisk modellering, vilka framförallt är relaterade till de geometriska och mekaniska egenskaperna hos spricknätverket, speciellt vad gäller frågor om uppskalning och anisotropi. Syftet är även att adressera, genom numerisk modellering, de frågor som är resultat av den komplexa naturen hos spricksystem i berg (t ex frågan om kontinuum eller diskontinuum representation). Riktlinje för projektet har varit att förstå vilken fysisk roll som sprickorna spelar för bergmassans mekaniska respons och använda det för att utveckla modelleringemetodiken. Bergmassan ses som bestående av en uppsättning diskreta sprickor inbäddade i en bergmatrix med uniforma elastiska egenskaper.

Den första fasen i utvecklingen är bestämning av ekvivalenta effektiva elastiska egenskaper (dvs Youngs elasticitetsmodul och Poissons tal eller deformationstensorn i det generella fallet) för ett ”bergmasse-prov” i DFN-skala. De teoretiska delarna av utvecklingsarbetet publicerades i *Journal of Geophysical Research* (Davy et al. 2018) under projektet. De bygger på en ackumulering, i bergmasseskala, av skjuv- och normalrörelserna från varje enskild spricka i DFN-populationen.

I skalan för enskilda sprickor etableras först förhållandet mellan belastningen på ränderna, sprickornas rörelser och den resulterande deformationen i bergmasseskalan. Sprickornas materialmodell baseras på Coulombs konstitutiva modell för skjuvbrott, i vilken normalrörelsen är proportionell mot normalstyvheten k_n , och sprickans skjuvrörelse är proportionell mot skjuvstyvheten k_s , upp till en kritisk skjuvspänning och glider efter att detta tröskelvärde har uppnåtts. Både normal- och skjuvstyvhet kan vara beroende av sprickans storlek eller orientering, eller på spänningsförhållandet.

Den första viktiga frågan gäller hur stor andel av motståndet som ska utgöras av sprickplanen respektive av omgivande bergets matrix. Det relativa bidraget från dessa två delar beror på en kombination av sprickans storlek, omgivande bergets deformationsmodul och sprickans skjuvstyvhet k_s . En specifik längdskala definieras, benämnd ”styvhetslängd” l_s , från kvoten mellan det intakta bergets deformationsmodul E_m och sprickans skjuvstyvhet k_s . Det visas att sprickor som är mycket större än styvhetslängden ligger i en regim dominerad av sprickstyvheten, medan sprickor som är mindre än styvhetslängden ligger i en regim dominerad av ”matrixstyvheten” (benämnd k_m), där k_m är proportionell mot E_m/l och l är sprickstorleken.

Ett samband etableras för att summera bidragen från varje enskild spricka till deformationen i bergmasseskala. En effektiv teori tillämpas för att ta hänsyn till interaktionen mellan sprickor när sprickintensiteten i spricknätverket är högt. Alla teoretiska samband som utvecklats har kontrollerats med numeriska simuleringar gjorda med programmet 3DEC. I slutet av utvecklingsfasen, kan dessa definierade samband användas till att beräkna de elastiska effektiva egenskaperna hos varje bergmassa med vilket spricknätverk som helst. Metodiken är tillämpad på flera fall, för att visa på dess kapacitet att prediktera och att relatera uppskalning och anisotropi hos bergmassans egenskaper till skala och anisotropin hos DFN-modellerna.

Förutom studien avseende bergmassans skala och effektiva elastiska egenskaper så analyseras spänningsvariationen – spänningarna fluktuation på en skala som är mindre än den skala som de effektiva egenskaperna beräknas för – i förhållande till den spatiala fördelningen av sprickorna i bergmassan. Ett flertal tensorer och skalärer används som indikatorer och jämförs. Dessa analyser är del av en preliminär metodologiutvecklingsfas och kommer att fortsätta mot att prediktera intensiteten i spänningsvariationen, bergmassans hållfasthet och mot att optimera representationen av bergmassan, som en kombination av effektiva egenskaper och diskreta sprickor.

Contents

1	Introduction	7
2	Rock mass and DFN description	9
3	Numerical setup	11
4	Isolated fracture	13
4.1	Constitutive frictionless and Coulomb slip models	13
4.2	Stress-displacement relation for a general case	16
5	Effective elastic properties	19
5.1	Results from simulations	19
5.2	Fracture displacement to specimen volume	20
5.3	From one fracture to a population of fractures	21
5.3.1	Framework	21
5.3.2	Interactions and effective theory	22
5.3.3	Simplified solutions	24
5.3.4	Comparison with other approaches – empirical methods for rock mass classification	27
5.3.5	Comparison with other approaches – DFN approach	27
6	Stress fluctuations	29
6.1	Origin of stress fluctuations	29
6.2	Stress fluctuation indicators	30
6.2.1	Scale	30
6.2.2	Scalar indicators	31
6.2.3	Tensorial indicators	32
6.3	Results	33
6.3.1	Exploratory study – isolated fracture	33
6.3.2	Exploratory study – DFN scale	34
6.3.3	Exploratory study – fracture vicinity	35
7	Applying the methodology to multiscale DFN	39
7.1	Discrete and effective representation for a DFN	39
7.2	From DFN discrete to effective representation	40
7.2.1	Description of required input	40
7.2.2	Description of the output	40
7.2.3	Sensitivity to order	40
7.3	Application to DFN with a power-law size distribution	41
7.3.1	DFN model and setup	41
7.3.2	Effective properties below L_c	43
7.3.3	Rock mass macroscopic elastic properties	44
7.3.4	Stress fluctuations	45
7.3.5	Focus on large fractures	48
7.3.6	Summary and recommendation	49
7.4	Test cases application	50
7.4.1	FFM01 Fracture Domain at Forsmark	50
8	Conclusions	53
	References	55
	Appendix Rock mass classification systems	59

1 Introduction

This report summarizes the work performed over the period March 2016 to June 2019 relative to the development of a methodology to derive rock mass effective elastic properties from a Discrete Fracture Network modelling approach.

For the Forsmark future deep disposal, getting such properties at appropriate scales is required at several stages of the design and safety assessment program of the future repository (Andersson et al. 2002, Staub et al. 2002, Hakami et al. 2021). This, for example, includes modelling of in situ stresses with their spatial and scaling organization, estimating locally the rock quality for constructability and integrating local stress distributions with the flow and transport modelling (primarily through the relationship between fracture loading stress and fracture transmissivity).

The derivation of rock mass effective mechanical properties raises issues related to the weakening role of fractures. Estimating the impact of fractures is particularly critical in the context of nuclear waste disposal but common to many other geotechnical applications. The fractures are the rock heterogeneities whose impact on rock strength and deformability is dominant (Davy et al. 2018). One of the main difficulties for rock masses like those at the Forsmark site, is that the distribution of the fractures is very complex, with a wide range of spatial scales involved and a density which is highly variable in space; therefore, making the fracture pattern modelling very challenging. In these systems, the fracture size distribution typically spreads orders of magnitude over which the relative number of smaller structures is much larger than the number of the larger structures, but the impact of individual fractures is strongly correlated with their sizes, such that the large structures may dominate the rock mass properties at large scales. Another major issue is that it is not possible to perform any direct and in situ evaluation of the mechanical properties at dimensions consistent with all the modelling needs. Laboratory tests are limited to typical core or slightly larger dimensions, or to samples containing single fractures (e.g., direct shear tests). Larger dimensions, from several meters to hundreds of meters, where the rock mass contains a large population of discrete fractures, cannot be directly evaluated, hence, assessment of their properties relies mostly on theoretical, analytical, and numerical modelling.

The common practice for standard geotechnical work is to characterize the rock mass based on empirical classifications charts (Rock Mass Classification – RMC), whose potential advantage is the simplicity of application but whose strong disadvantage is the oversimplification of the fracture pattern description, so that their application range is limited. The pro arguments for using RMC are that they are derived from practical observations and simple experience-based rules. Also, they are flexible and effective for construction and support design and for scoping calculations at early stages of projects when there is poor knowledge of the system. The cons are that they are not well-suited for safety analysis for nuclear waste disposal where long-term behaviour, coupled processes, anisotropy and scale dependency can play a major role.

The level of accuracy and understanding required for the long-term nuclear waste storage has motivated the development of the present methodology, based on a detailed description of the rock mass as a rock with discrete and widely distributed fractures. The method development relies both on analytical development and numerical modelling of synthetic rock specimens defined by discrete fractures embedded in a rock matrix.

The objectives of current study are to: *i*) improve the understanding of the role played by the fractures on the mechanical behaviour of the rock mass, *ii*) evaluate the macroscopic effective properties and the local stress fluctuations, *iii*) derive guidelines adapted to conditions similar to those at the Forsmark site and emphasize the critical aspects and *iv*) derive the workflow for applying the methodology to a full or partial part of the DFN, with a particular attention to the scale and anisotropy issues.

The report is organized as follows. The assumptions relative to the elementary description of the rock mass as an intact rock into which a discrete fracture population (the DFN) is embedded are recalled in Section 2. The numerical setup common to most of the numerical simulations is introduced in Section 3. Section 4 deals with the mechanical behaviour and response in terms of displacement (normal and shear) of a single fracture. The derivation of the effective elastic properties at the DFN scale is developed in Section 5. The two previous sections include the main elements of the article

published in the Journal of Geophysical Research (Davy et al. 2018). The stress fluctuations within a fractured rock mass are analysed in Section 6. Section 7 describes the application of the methodology to multiscale DFN. It includes a short description of the workflow for deriving the effective properties, an analysis of stress fluctuations variations as a function of the transition scale between effective and explicit representation of the fractures and a test case (FFM01 unit in Forsmark). This section also highlights the scale effects and anisotropy of effective elastic properties. These sections are followed by a summary and discussion, and a conclusions and perspectives section.

2 Rock mass and DFN description

In this study, the rock mass is defined as an isotropic homogenous rock matrix into which discrete fractures are embedded. The fractures are disc-shaped and therefore, each fracture is defined by a diameter (named fracture size in this report), an orientation and a position. In the following we successively numerically build and test several rock masses based on different DFN models (Table 2-1).

A detailed description of the DFN modelling framework adapted for the present work can be found in Selroos et al. (2021). We briefly introduce here the fracture density distribution model, n_{3D} , the DFN total fracture surface per unit volume P_{32} and the DFN percolation parameter p .

The fracture density distribution, $n_{3D}(P)$, is the basis of the fracture system description. It defines a quantitative measure of the fracture population, basically how many fractures per unit volume V , according to a set of parameters P :

$$n_{3D}(P) = \frac{1}{V} \lim_{dP \rightarrow 0} \frac{\sum_{f(P'; P' \in [P, P+dP])} \pi_f(V)}{dP} \quad (2-1)$$

The sum is over the fractures f whose parameters p' are in the range $[P, P + dP]$. Each fracture f contributes as $\pi_f(V)$, the probability of the fracture to belong to the 3D sampling system of volume V . It is very often convenient to calculate the density parameters for only a subset of parameters, independently from the others. This comes to integrate $n_{3D}(P)$ over the parameters that are not considered.

The DFN total fracture surface per unit volume P_{32} for fractures over a fracture size range $[l_{lo}; l_{up}]$ is:

$$P_{32}(l_{lo}, l_{up}) = \int_{l_{lo}}^{l_{up}} n_{3D}(l) \frac{\pi}{4} l^2 dl \quad (2-2)$$

Where here $n_{3D}(l)$ is the fracture size density distribution integrated over all parameters except the size and l_{min} and l_{max} the integration boundaries.

A very important metric of the DFN density distribution, the percolation parameter p , is proportional to the third order moment of the fracture size density distribution:

$$p(l_{lo}, l_{up}) = \int_{l_{lo}}^{l_{up}} n_{3D}(l) \frac{\pi^2}{8} l^3 dl \quad (2-3)$$

When applied to the DFN models defined by a wide range of fracture sizes (e.g., the power-law models with exponent in the range -3 to -4), the dependency of P_{32} and p on the boundaries of the fracture size density distribution are key components of the DFN scale properties. For instance, p , this dimensionless moment of the distribution, is a cornerstone of the percolation theory and thus called the percolation parameter (Bour and Davy 1998, de Dreuzy et al. 2000, Barker 2018). It is primary a statistical indicator of the degree of connectivity within a DFN and, therefore, an essential indicator for all flow applications.

The rock mass and DFN models used in the following are listed in Table 2-1. The first type of fracture network and rock mass specimen is the “isolated fracture” case. The second set encompass several DFN models all with constant sizes, the $n01$ to $n12$ test cases. The different combinations of sizes and densities P_{32} define percolation parameter values from 0.7 to 15. The last set refers to DFN models with a power law size density distribution $n_{3D}(l) = \alpha_{3D} \cdot l^{-a_{3D}}$, with $a_{3D} = 4$ and $\alpha_{3D} = 2.26$. For the simulations, the low boundary of the size distribution (l_{min}) is set to 0.2 or 0.4 meters.

Table 2-1. Summary of the DFN models and parameters.

Name	type	Size l (m)	P_{32} (m ² /m ³)	ρ (-)
isolated	Single fracture	1		
<i>n01</i>	Constant sizes	0.5	1	0.785
<i>n02</i>	Constant sizes	1	1	1.571
<i>n03</i>	Constant sizes	0.5	2	1.571
<i>n04</i>	Constant sizes	0.5	3	2.356
<i>n05</i>	Constant sizes	1	2	3.142
<i>n06</i>	Constant sizes	2	1	3.142
<i>n08</i>	Constant sizes	1	3	4.712
<i>n09</i>	Constant sizes	2	2	6.283
<i>n10</i>	Constant sizes	1	5	7.854
<i>n11</i>	Constant sizes	2	3	9.425
<i>n12</i>	Constant sizes	2	5	15.708
<i>pl</i>	Power-law	$0.4 \leq l \leq 4$ $n_{3d}(l) = \alpha_{3d} \cdot l^{-\alpha_{3d}}$ $\alpha_{3d} = 4, \alpha_{3d} = 2.26$	4	
<i>pl</i> $l_{min} = 0.2$	Power-law	$0.2 \leq l \leq 4$ $n_{3d}(l) = \alpha_{3d} \cdot l^{-\alpha_{3d}}$ $\alpha_{3d} = 4, \alpha_{3d} = 2.26$	8.44	

The fracture mechanical model is the Coulomb slip law (Equation (4-2) and (4-3)). A variant of the model is introduced by coupling the fracture normal and shear stiffnesses to the normal stress on the fracture (Table 2-2).

Table 2-2. Summary of fracture mechanical properties.

Model name	Reference	$k_n = (GPa/m)$	$k_s = (GPa/m)$
Coulomb slip	(Davy et al. 2018)	$k_n = 12600$	0, 12 or 72
Modified Coulomb slip	(Mas Ivars et al. 2015, Darcel et al. 2018)	$k_n(\sigma_n) = 2.28 \sigma_n^{0.822} \times 10^6$	$k_s(\sigma_n) = 46.55 \sigma_n^{0.4039} \times 10^6$

Finally, the isotropic and homogenous intact rock around the fractures is simply defined by a Young's modulus E_m and Poisson's ratio ν_m , with typical values in the table below.

Table 2-3. Intact rock mechanical properties.

Reference	E_m (GPa)	ν_m (-)
(Darcel et al. 2018)	76	0.25
(Davy et al. 2018)	53	0.25
Section 7	76.9	0.23

3 Numerical setup

The reference Synthetic Rock Mass (SRM) specimen is parallelepipedal, of a height of 8 m and side 4 by 4 m for the $n01$ to $n12$ DFN cases. For the $p/$ DFN cases the SRM specimen are cubic of edge lengths of 6 m.

The numerical simulations are performed with 3DEC© version 5.2 (Itasca 2016). 3DEC is a three-dimensional numerical software based on the distinct element method (DEM) for discontinuum modelling. It is based on a Lagrangian calculation scheme. Following the mesh generation process within 3DEC, the initial specimen is first defined as one single block, which is progressively cut into smaller and smaller blocks when fractures are added to the sample. The block assembly is then meshed block by block with a target zone size (Figure 3-1), which is 0.2 m for most of the simulations presented in this report.

Elastic mechanical properties are assigned in the zones. The elastic properties of the fractures are assigned to the area fraction corresponding to the fractures at the interfaces between the blocks.

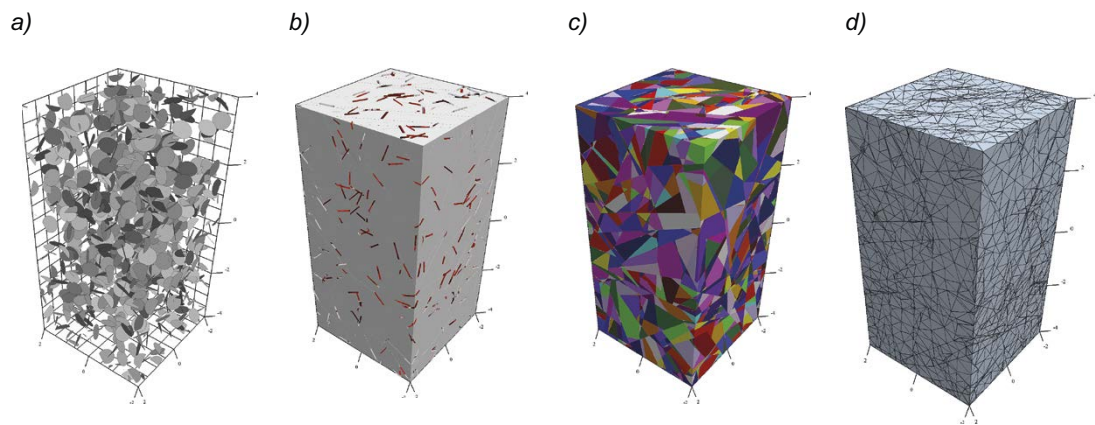


Figure 3-1. From left to right, steps of the SRM specimen construction with a) DFN, b) specimen dimensions, c) blocks and d) zones.

SRM specimen are loaded such that the maximum principal stress σ_1 (with a convention of positive compressive stress) is vertical (z direction) and the confinement is isotropic in the lateral directions, with $\sigma_2 = \sigma_3 = \sigma_c$ (x and y directions). The loading and resulting stress state are controlled by a servo-control process which imposes the strain rate components in the directions perpendicular to the faces: the top and bottom faces have fixed velocities in the z direction, the left and right faces (normal \vec{x}) have fixed x -component velocity and the front and back faces have a fixed y -component of the velocity. For the SRM generic tests, the stresses are $\sigma_1 = 3.0 \times 10^{-2} \text{ MPa}$ and $\sigma_c = 1.0 \times 10^{-2} \text{ MPa}$.

The loading path is done in two steps. First the loading stress (through the servo control over the strain rates) is increased up to σ_c the confinement stress on all sides of the SRM specimen. Second, the lateral confinement is kept constant while the vertical stress is increased up to the target value σ_1 . The simulations are performed in quasi-static conditions and small deformation mode.

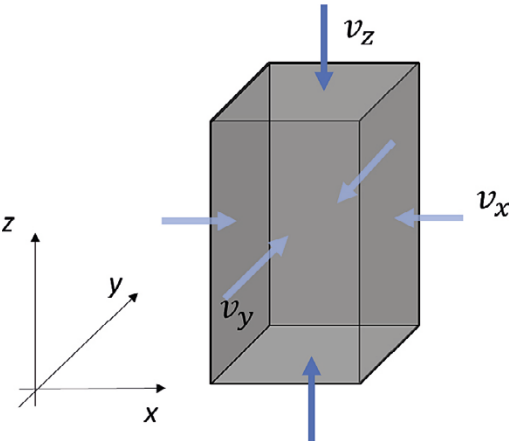


Figure 3-2. SRM specimen. Sketch for boundary conditions with fixed velocities in the directions perpendicular to the faces.

4 Isolated fracture

4.1 Constitutive frictionless and Coulomb slip models

We describe first the behaviour of an isolated fracture embedded in an intact and isotropic elastic material as sketched in Figure 4-1.

The first fracture constitutive model is the *frictionless* or *free-slipping* model, where the fracture shear displacement is only limited by the rock matrix around the fracture and where the in-plane fracture resistance is null (Sneddon and Lowengrub 1969, Kachanov and Sevostianov 2013). In this case the shear displacement profile has a parabolic shape and its average value \bar{t} is:

$$\bar{t} = \frac{\tau_R}{\frac{3\pi^{1-\frac{\nu_m}{2}} E_m}{8(1-\nu_m^2) l}} \quad (4-1)$$

where τ_R is the shear stress on the fracture plane deduced from the remote stress conditions.

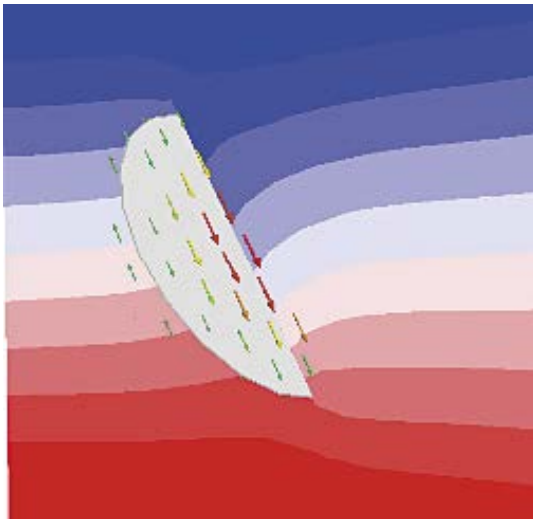


Figure 4-1. Sketch of an isolated fracture with in-plane shear displacement and vertical displacement of the surrounding matrix for a fracture loaded vertically.

The second fracture rheological model (Figure 4-2), the Coulomb slip model, has an elastic resistance in the fracture plane (Equation (4-2)) controlled by a shear stiffness parameter k_s , and a maximum shear stress threshold τ_c above which the fracture reaches a free-slipping state:

$$\tau_f = k_s \cdot t \text{ if } \tau_f < \tau_c \quad (4-2)$$

$$\tau_f = \tau_c \text{ otherwise}$$

with τ_f the shear stress in the fracture plane and t the shear displacement.

The maximum shear stress threshold τ_c is defined by a classical Coulomb like criterion (Equation (4-3)):

$$\tau_c = \sigma_n \cdot \tan(\phi) + C \quad (4-3)$$

where ϕ is the friction angle, C is the cohesion and σ_n is the fracture normal stress.

The normal displacement (u_n) on the fracture plane is elastic and controlled by the fracture normal stiffness k_n and normal stress σ_n :

$$\sigma_n = k_n \cdot u_n \quad (4-4)$$

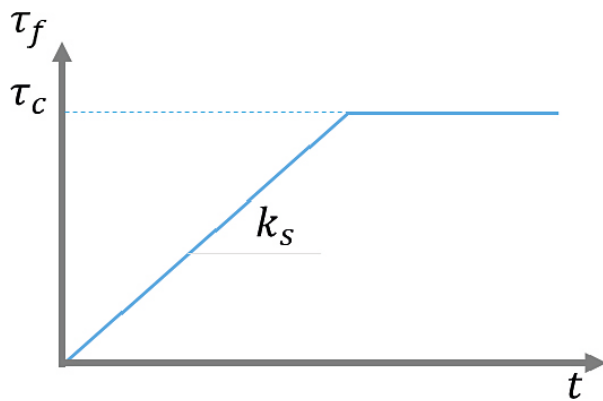


Figure 4-2. Fracture Coulomb slip model with $\tau_c = \sigma_n \cdot \tan(\phi) + C$.

For critically stressed fractures (i.e., if $\tau_f = \tau_c$) one can consider an additional normal displacement due to the dilation term, $u_{n,dil}$, as defined in Figure 4-3.

The shear stress τ_f and the normal stress σ_n applied on a fracture of normal n are defined by:

$$\tau_f = \mathbf{n}^T \cdot \bar{\sigma} \cdot \mathbf{s} \quad (4-5)$$

with

$$\mathbf{s} = s_g / \|s_g\|$$

$$s_g = \mathbf{n}^T \cdot \sigma \cdot (1 - \mathbf{n}^T \cdot \mathbf{n}) \quad (4-6)$$

and

$$\sigma_n = \mathbf{n}^T \cdot \bar{\sigma} \cdot \mathbf{n} \quad (4-7)$$

where $\bar{\sigma}$ is the stress tensor and s is the unit vector of the shear direction.

The frictionless regime can be seen as an end-member of the Coulomb slip model, when $\tau_f = \tau_c = 0$, so keeping τ_f equal to zero or having $k_s = 0$ in Equation (4-2).

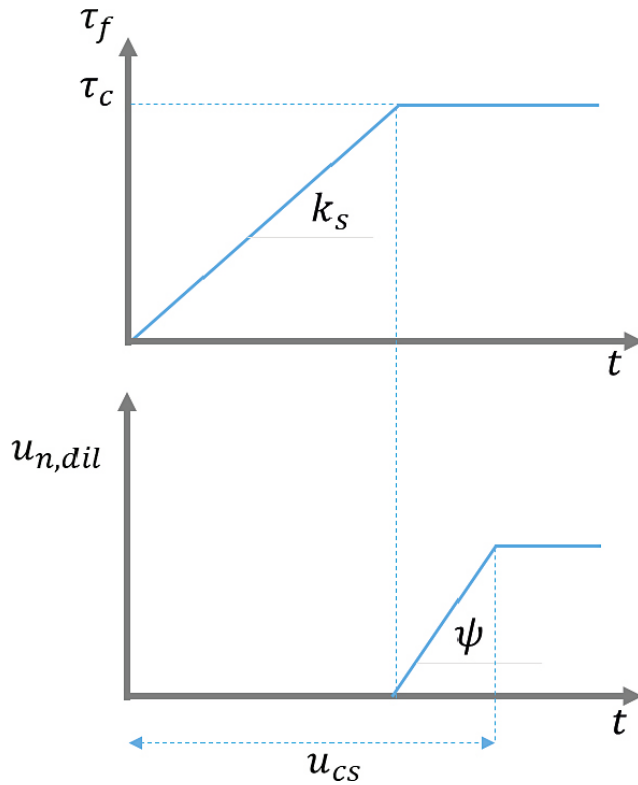


Figure 4-3. $u_{n,dil}$ dilational component of normal displacement, with two parameters, the dilation angle ψ and the critical displacement u_{cs} .

4.2 Stress-displacement relation for a general case

An isolated frictionless disk-shaped fracture under loading conditions displays a parabolic shear displacement profile $t(r)$ (Kachanov and Sevostianov 2013) which forms a maximum displacement at the fracture center to a null displacement at the fracture tip, defined by Equation (4-8):

$$t(r) = \frac{4(1-\nu_m^2)}{\pi(1-\frac{\nu_m^2}{2})} \tau_m l_f / E_m \sqrt{1 - \left(\frac{2r}{l_f}\right)^2} \quad (4-8)$$

where ν_m and E_m are the Poisson's ratio and Young's modulus of the intact rock (matrix), respectively, τ_m is the shear stress around the fracture and l_f the size of the fracture. The average shear displacement t , as defined in Equation (4-9), is two thirds of the displacement at the fracture center $t(r=0)$:

$$t = \frac{\tau_m}{k_m} \quad (4-9)$$

and

$$k_m = \frac{3\pi}{8} \cdot \frac{1-\nu_m/2}{1-\nu_m^2} \cdot \frac{E_m}{l_f} \quad (4-10)$$

Following Davy et al. (2018), k_m is called the matrix-fracture stiffness. Davy et al. (2018) demonstrate how the former expression can be generalized to the "fracture with friction" case (i.e., $k_s > 0$ and $\tau_p > 0$). It is shown that for these conditions:

$$\begin{aligned} t &= \frac{\tau}{k_s + k_m} & \text{if } \tau \leq \tau_p^* \\ t &= \frac{\tau - \tau_p}{k_m} & \text{if } \tau > \tau_p^* \end{aligned} \quad (4-11)$$

$$\tau_p^* = \frac{k_s + k_m}{k_s} \tau_p$$

where τ_p is the fracture friction threshold.

The relationship between fracture shear displacement t , fracture shear stress τ_f and remote stress τ is plotted in Figure 4-4. It emphasizes the remote stress partitioning between the elastic resistance of the fracture surface (with k_s) and the elastic resistances of the matrix around the fracture (with k_m). The plots in Figure 4-4 emphasize the potential shift between the fracture and the remote shear stresses. τ_p^* is the shear threshold of the remote stress necessary to reach the fracture shear threshold for slipping. The discrepancy between τ and τ_f reflects the intensity of the matrix-stiffness component with regards to the fracture stiffness itself. If $k_m \gg k_s$ the remote stress necessary to reach the slipping regime is much larger than the fracture friction (τ_c). On the contrary, if k_m is negligible compared to k_s , the critical remote shear stress converges to the predefined fracture friction threshold (τ_p).

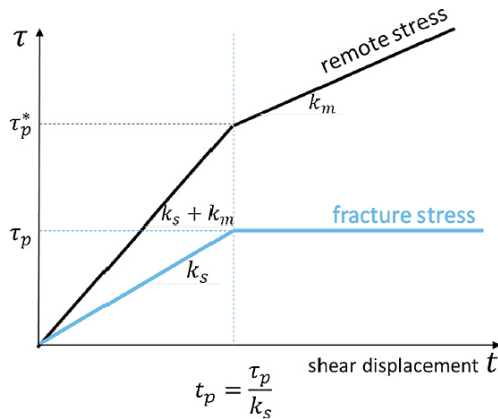


Figure 4-4. The relationship between shear displacement t and remote stress τ (black curve) is defined by Equation (4-11) and between t and the fracture shear stress (τ_f) by Equation (4-2). Note: figure modified from Davy et al. (2018).

The role played by the matrix and fracture-matrix stiffness in the prediction of the slipping potential of a fracture is further illustrated in Figure 4-5.

Simulations are performed to validate Equation (4-11), for different shearing and slipping conditions. The results are plotted in Figure 4-6. The numerical experiment consists of a single fracture embedded in a rock matrix and loaded with a maximum principal stress in the vertical direction. The angle θ (the horizontal axis in the plot) is the angle between the fracture plane and the maximum principal stress direction (so here $\theta = 0$ refers to a vertical fracture and $\theta = 90^\circ$ to a horizontal fracture). For conditions similar to the frictionless case ($\equiv k_s = 0$) the displacement is fully defined by Equation (4-9), there is no threshold effect between slipping and elastic shearing. For conditions where the fracture shear stiffness is increasing, the difference between the remote and fracture shear stress gradually decreases until the latter becomes dominant (blue curve in the figure).

Depending on the combination between fracture and rock mechanical parameters and the shear stress applied on a fracture (itself dependent on the respective fracture and stress field orientation), two main regimes arise at the fracture scale, one dominated by the shear (and k_s) and one dominated by the slipping (and k_m). Depending on the size of a fracture, one or the other can be dominant. Thus, we define a typical fracture size scale, the “stiffness length scale” l_s as the fracture size for which $k_m = k_s$:

$$l_s = \frac{k_m \cdot l_f}{k_s} = \frac{3\pi}{8} \cdot \frac{1-\nu_m/2}{1-\nu_m^2} \cdot \frac{E_m}{k_s} \quad (4-12)$$

Fractures much larger than l_s show a shear (and k_s) regime while fractures much smaller than l_s show a slipping (k_m) regime.

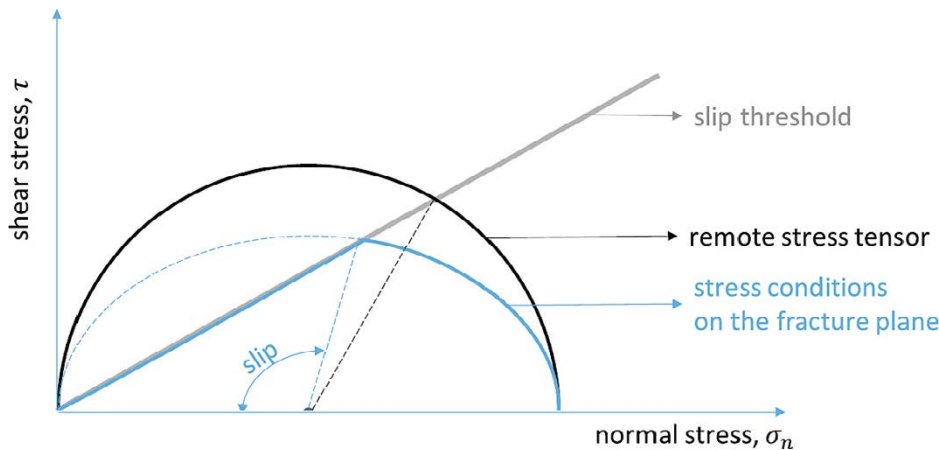


Figure 4-5. Slip conditions in a Mohr-Coulomb stress diagram (shear versus normal stress). The black half-circle reflects the shear and normal stress components of the remote stress tensor relative to the fracture orientation (as classically expressed in a Mohr-Coulomb diagram). The grey straight line is the friction (or slip threshold) envelop. The blue half-ellipsoid shows the stress conditions, in a fracture plane resulting from the remote stress and fracture-matrix stiffness. The dashed blue line indicates the range of fracture angles for which slipping regime will be reached. Note: figure from Figure 8 in Davy et al. (2018).

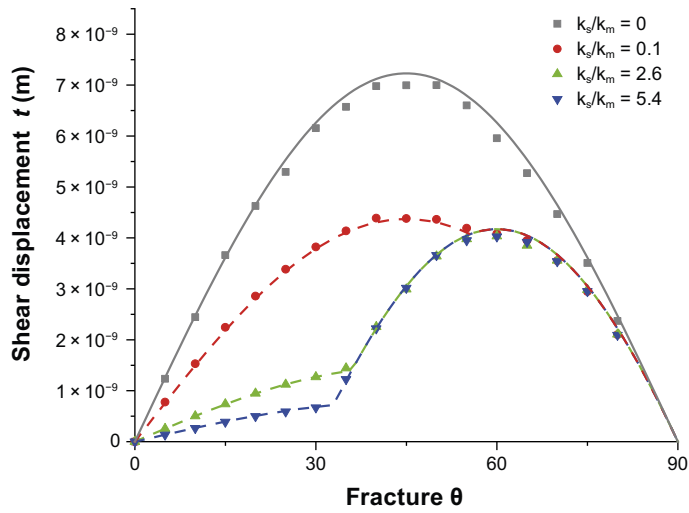


Figure 4-6. Plot of the shear displacement t – at the fracture center position – versus the fracture orientation θ (figure modified from Figure 8 in Davy et al. (2018)). The different colors (symbols and curves) correspond to different ratio of k_s/k_m as defined in the legend, constant friction angle is equal to $\phi = 30^\circ$ and the null cohesion. The dots are calculated from numerical simulations with 3DEC and the dashed lines from Equation (4-11). The break in the curves marks the angle limit between non-slipping and slipping conditions; the larger the k_s is, the smaller the angle limit is.

5 Effective elastic properties

This chapter is the core of the DFN based approach to assessing the effective mechanical properties. The objective is to define, over a given rock mass scale, analytical relationships between a DFN, or the statistical parameters of a DFN, and the effective rock mass mechanical properties. The main results of the approach have been published in Davy et al. (2018). Here we resume the main steps and outstanding results.

5.1 Results from simulations

Several SRM specimens, based on the realizations of the DFN models $n01$ to $n12$ (Table 2-1), are subjected to loading tests such that the apparent Young's modulus and Poisson's ratio can be assessed. The estimated properties are E_{zz} (the Young's modulus measured from a change of stress in the vertical direction while keeping lateral confinement constant) and the Poisson's ratio ($\nu_{xy} = \nu_{yx}$). Since the tested DFN models are statistically isotropic (no preferential orientation for the fractures), no anisotropy is expected in the SRM scale apparent elastic properties, consequently, $E = E_{zz}$ and $\nu = \nu_{xy}$. With this set of numerical tests, the combined effect of fracture sizes, density and mechanical properties is hence first treated for isotropic conditions. However, the effects of anisotropy due to the DFN geometry or to the mechanical properties is treated in the generalization of the approach (Section 5.3.2).

The evolution of the apparent Modulus is plotted as function of the two geometrical indicators of the DFN, the DFN percolation parameter p (Equation (2-3)) in Figure 5-1a and the DFN density P_{32} (Equation (2-2)) in Figure 5-1b.

Figure 5-1 emphasizes a general decrease of E as a result of an increase of the amount of fractures in the SRM specimen (at a given size, more fractures in a unit volume leads directly to increase of both P_{32} and p) which is an observation consistent with empirical knowledge (see Appendix). The largest variations in E is observed for $k_s = 0$ (53 GPa for the intact matrix down to almost 10 GPa) whereas it is much more limited for $k_s = 72$ GPa/m (down to 40 GPa for the rock mass). If the fracture stiffness is high, the resulting displacement is limited and; therefore, it will limit the impact of the DFN on the apparent properties.

For the case of $k_s = 0$, the decrease of E with p follows a single trend for all models combined (Figure 5-1a, black symbols) whereas the dispersion increases when k_s increases (especially for $k_s = 72$ GPa/m). However, the variation of E with P_{32} is less dispersed when k_s is at the highest.

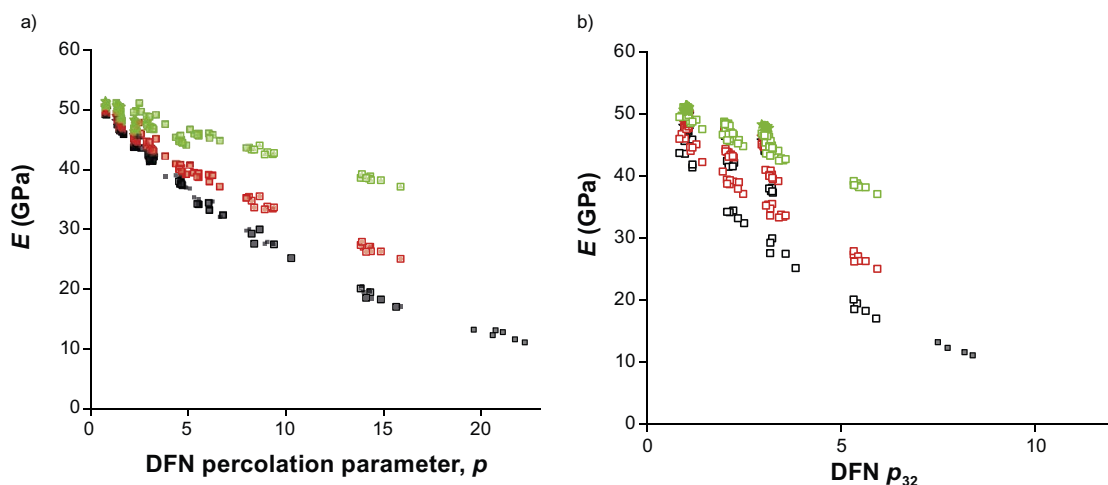


Figure 5-1. Estimation of the Young's Modulus at the SRM specimen scale deduced from numerical simulations performed for the $n01$ to $n12$ DFN models (Table 2-1), plotted as function of a) the DFN model percolation parameter and b) the DFN model P_{32} density. For both plots, $k_s = 0$ (black symbols), $k_s = 12$ GPa/m (red symbols) and $k_s = 72$ GPa/m (green symbols).

Note that all the results shown in this section have been obtained with a value of k_n 175–1 000 times larger than k_s , precluding any significant contribution of the normal displacement compared to shear displacement.

In the next sections, we propose an analytical development to explain the abovementioned observations and to quantitatively define the relationship between DFN geometrical and mechanical properties with the effective elastic properties, by accounting for the contribution of each fracture explicitly.

5.2 Fracture displacement to specimen volume

The contribution of the fracture displacement to the specimen scale deformation is explained by Davy et al. (2018). This section and Sections 5.3.1 to 5.3.3 are adapted from Davy et al. (2018). Let's consider a fracture of normal vector n , surface S_f , displacement t (with a shear displacement t_s and a normal displacement u_n) (Figure 5-2).

We first derive the expression considering only the fracture shear displacement t . The contribution of the fracture to the displacement of a specific boundary X (t_X) is obtained by projecting and integrating the displacement field on X (see for instance Kachanov (1993) and Kachanov and Sevostianov (2013)) as:

$$\mathbf{t}_X = (\mathbf{n} \cdot \mathbf{n}_x) \frac{\iint_{S_f} \mathbf{t} dS}{S_X} \quad (5-1)$$

where S_X and n_x are the surface area and the normal vector to X and S is the plane that includes the fracture. The expression is used to calculate the deformation of a sample, for which X is a boundary, and whose volume V is $V = S_X \cdot l_x$ with l_x being the dimension perpendicular to X (i.e., in the direction n_x). The contribution of the fracture to the deformation component ϵ_{xy} , where x refers to the surface X and y to a direction vector n_y , is:

$$\epsilon_{xy} = \frac{t_X \cdot n_y}{l_x} = (\mathbf{n} \cdot \mathbf{n}_x) \frac{\iint_{S_f} (\mathbf{t} \cdot \mathbf{n}_y) dS}{V} \quad (5-2)$$

The expression is generally expressed with the average displacement (\bar{t}) in the fracture disk:

$$\epsilon_{xy} = (\mathbf{n} \cdot \mathbf{n}_x) \frac{S_f}{V} (\bar{\mathbf{t}} \cdot \mathbf{n}_y) \quad (5-3)$$

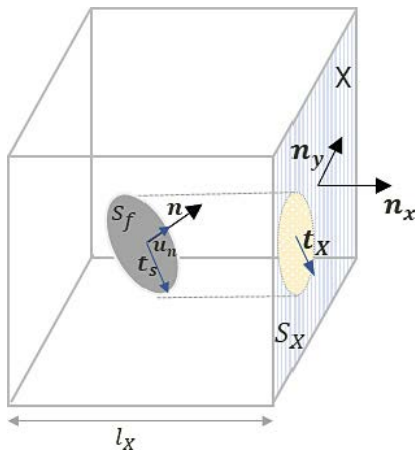


Figure 5-2. Illustration of the relation between the fracture displacement and the projection at the specimen volume scale. The X surface is highlighted as a blue striped area over the total surface S_X .

5.3 From one fracture to a population of fractures

5.3.1 Framework

The DFN scale derivation of effective elastic properties (Young's modulus E and Poisson's ratio ν for an isotropic medium or full compliance tensor \bar{C} in a general case) is based on the summation of the contribution of each individual fracture to the rock mass specimen scale boundaries. This is comparable to effective theories, that are generally written by incrementally adding elements to an effective medium whose properties are potentially iterated too during the incremental process. At each step i of the incremental process, the total deformation is the sum of two terms:

- the deformation of the damaged matrix, $(\epsilon)_{i-1}$, due to the remote stress tensor $\bar{\sigma}$ applied on the equivalent medium constituted of $(i-1)$ fractures with equivalent elastic properties $(E)_{i-1}$ and $(\nu)_{i-1}$,
- the deformation induced by the displacement on the additional i th fracture.

Following Equation (5-3), the strain state at step i is defined by:

$$(\epsilon_{xy})_i = (\epsilon_{xy})_{i-1} + (\mathbf{n}_i \cdot \mathbf{n}_x) \frac{S_i}{V} (\bar{\mathbf{t}}_i \cdot \mathbf{n}_y) \quad (5-4)$$

where S_i is the surface of the fracture i , \mathbf{n}_i is its normal, and $\bar{\mathbf{t}}_i$ is its displacement.

In the present context, the main assumptions of any effective theory aim at statistically evaluating the average displacement $\bar{\mathbf{t}}_i$, which depends on both the stress applied to the fracture, and the properties of the matrix. The former (stress) is controlled by the remote stress tensor $\bar{\sigma}$, and to some extent by the fluctuations of stresses induced by the $(i-1)$ fractures. To our knowledge, the role of stress fluctuations is not usually considered in effective theories; it will not be either directly here, but stress fluctuations are explored in Section 6. The latter (medium behaviour) is controlled by the matrix properties E_m and ν_m , which may be altered by the previous $(i-1)$ fractures to some extent.

The shear component of $\bar{\mathbf{t}}_i$ (t in Equation (4-11)) depends on 3 terms: the shear stress τ_i (Equation (4-5)) with \mathbf{s}_i the direction of shear (Equation (4-6)); the fracture shear stiffness k_{s_i} , which may depend on each fracture, and the local matrix-fracture stiffness k_{m_i} , which is a function of the elastic properties of the medium surrounding the i th fracture. With these assumptions, evaluating $\bar{\mathbf{t}}_i$ comes to assessing this latter term.

The normal component u_n of $\bar{\mathbf{t}}_i$ is simply equal to σ_n/k_n (Equation (4-4)).

For non-critically stressed fractures (i.e., $\tau \leq \tau^*$, see Equation (4-11)), we write, as an example, the eventual deformation term (ϵ_{xy}) obtained by summing the contribution of all fractures:

$$(\epsilon_{xy}) = (\epsilon_{xy})_m + \sum_i (\mathbf{n}_i \cdot \mathbf{n}_x) \frac{S_i}{V} \left(\left(\frac{\mathbf{n}_i^T \cdot \bar{\sigma} \cdot \mathbf{s}_i}{k_{s_i} + k_{m_i}} \mathbf{s}_i + \frac{\mathbf{n}_i^T \cdot \bar{\sigma} \cdot \mathbf{n}_i}{k_{n_i}} \mathbf{n}_i \right) \cdot \mathbf{n}_y \right) \quad (5-5)$$

With Equation (5-5), all the components of the strain tensor $\bar{\epsilon}$ can be computed and combined with any stress boundary conditions to derive the effective elastic properties (components of the compliance tensor and/or Young's modulus and Poisson's ratio for specific isotropic conditions).

If the effective medium has isotropic properties, the apparent Young's modulus and Poisson's ratio are derived from the general equation:

$$\epsilon_{ii} = \frac{1}{E} (\sigma_{ii} - \nu(\sigma_{jj} + \sigma_{kk})) \quad (5-6)$$

where i, j, k denote any x, y and z directions.

For an unconfined uniaxial compression σ along the x axis, the Young's modulus and Poisson's ratio are:

$$E = \frac{\sigma_{xx}}{\epsilon_{xx}} \quad (5-7)$$

$$\nu = \frac{-\epsilon_{zz}}{\epsilon_{xx}}$$

In any case, the total deformation is increased by the contribution of the fracture displacements, so that the effective Young's modulus is smaller than E_m , and the Poisson's ratio is larger than ν_m .

In the following, we consider several assumptions relative to property evolution (mainly the matrix-fracture stiffness term k_{m_i}) during the incremental process of Equation (5-5) and compare the predictions with direct numerical simulations from the series of models $n01$ to $n12$ (Table 2-1 and Section 3).

The general expression is:

$$\bar{\bar{\epsilon}} = \frac{1}{\bar{\bar{E}}} \bar{\bar{\sigma}} = \bar{\bar{C}} \bar{\bar{\sigma}} \quad (5-8)$$

where $\bar{\bar{C}}$ is the compliance tensor.

5.3.2 Interactions and effective theory

The simplest model is to consider that the medium is not damaged in the vicinity of the fracture, so that the elastic properties are those of the intact matrix E_m and ν_m (no-interaction model). This gives an expression of k_{m_i} similar to Equation (4-10):

$$k_{m_i} = \frac{3\pi}{8} \frac{1-\frac{\nu_m}{2}}{1-\nu_m^2} \frac{E_m}{l_i} \quad (5-9)$$

where l_i is the length of the i th fracture. The no-interaction model is a good description of systems with a low density of fractures, where fractures are, on average, far apart from each other, so that any new fracture is only surrounded by the intact elastic matrix and the contribution of each fracture to $(\epsilon_{xy})_i$ is independent of the others.

The effective medium theories (see the reviews in Kachanov (1987), Jaeger et al. (2007) and Guéguen and Kachanov (2012)) for the case of $k_s = 0$ approximate the interaction between fractures with different schemes, the most popular being the self-consistent theory (O'Connell and Budiansky 1974), and the differential scheme (Hashin 1988). Here we develop the differential scheme, which avoids some inconsistencies of the self-consistent theory at high crack densities (Bruner 1976). It basically considers that the i th fracture is surrounded by a damaged medium. Effective properties are those of the medium constituted by the $(i-1)$ fractures embedded in the initial intact rock. For isotropic conditions this writes:

$$k_{m_i} = \frac{3\pi}{8} \frac{1-\frac{\nu_{i-1}}{2}}{1-\nu_{i-1}^2} \frac{(E)_{i-1}}{l_i} \quad (5-10)$$

The effective medium theory predicts a final Young's modulus smaller than that of the no-interaction model. Indeed, fractures are then embedded in a softer matrix, thus entailing a larger displacement in the fractures.

Results predicted by the no-interaction (Equation (5-9)) and by the effective theory (Equation (5-10)) are compared with the results of the numerical simulations of the models presented in Figure 5-1, Figure 5-3 and Figure 5-4. For relatively high values of the normalized Young's modulus (normalized by E_m , Young's modulus of the intact rock), the difference between the no-interaction and effective case is minimal and the effective modulus predicted by both models closely match with the simulations. When the effective moduli decrease (by increasing the amount of fractures in the DFN, so the density), the discrepancy with the no-interaction model increases (Figure 5-3a) while the adequacy with the effective theory model remains good, although the latter slightly underestimates the result (Figure 5-4a). The comparison between simulations and analytical models is also performed for the Poisson's ratio, in Figure 5-3b and Figure 5-4b. Increasing the DFN density tends to increase the Poisson's ratio. The prediction based on the effective theory avoids the discrepancies observed with the no-interaction model for the highest values of effective Poisson's ratio and overall, the prediction tends to slightly overestimate the effective Poisson's ratio value.

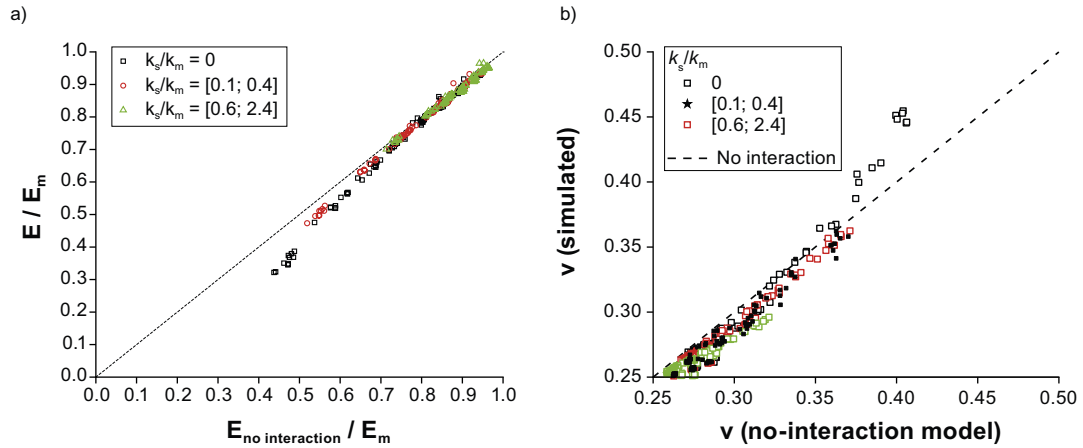


Figure 5-3. Young's modulus (left) and Poisson's ratio (right) calculated with 3DEC for all the cases shown in Table 2-1, as a function of the no-interaction model estimate. The dashed line shows the prediction by the no-interaction model (Davy et al. 2018).

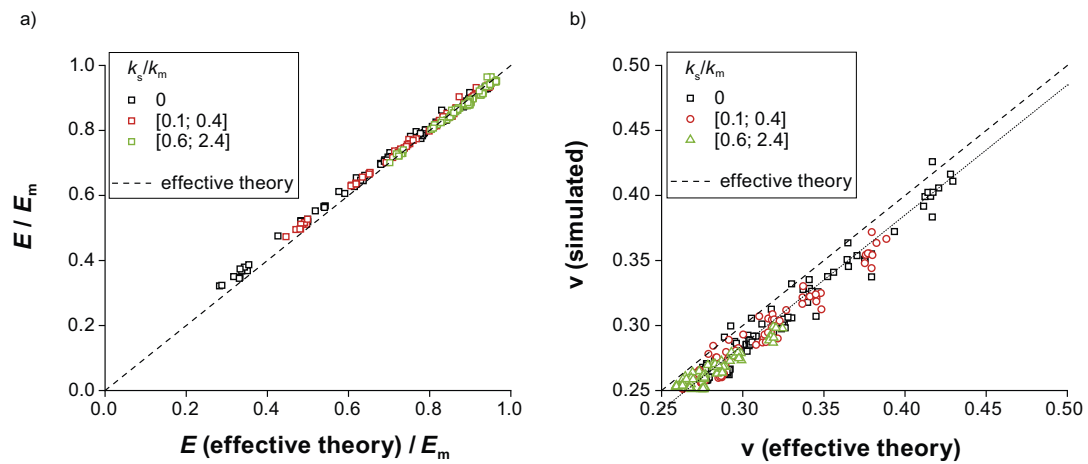


Figure 5-4. Young's modulus (left) and Poisson's ratio (right) calculated with 3DEC for all the cases shown in Table 2-1, as a function of the effective theory estimate. The dashed line shows the prediction $y = x$. The dotted line in the Poisson's ratio graph is $y = x - 0.15$. Modified from Davy et al. (2018).

The effective theory model (Equation (5-10) and (5-5)) satisfactorily predicts the evolution of the effective Young's modulus and Poisson's ratio. It is further used as a basis to analyse which components of the DFN geometrical and mechanical properties, together with the mechanical properties of the intact rock (or matrix), are dominant for specific configurations.

When applying the calculation in the general case (Section 7), the resulting effective elastic properties may have tensorial expression if the anisotropy is significant. In this case, the Young's modulus in Equation (5-10) and Equation (5-5) is taken as the harmonic average of the directional moduli (E_{xx} , E_{yy} , and E_{zz}).

5.3.3 Simplified solutions

The effective theory, as defined in the general Equations (5-10) and (5-5), is the basis of the effective elastic property derivation from a DFN approach. We review here several cases where simplifications can be done. The proposed formulations are expressed considering that fracture sizes and orientations are not correlated. The expressions are also valid if the shear and normal stiffnesses k_s and k^n are dependent on fracture size or normal stress.

Case $k_m(l) \gg k_s$ or frictionless case

For the frictionless case, we can demonstrate that the effective theory based effective Modulus E_{eff} is:

$$E_{eff} = E_m \exp\left(-\frac{\frac{2}{\pi}F_\theta}{N(v_m)}p\right) \quad (5-11)$$

$$N(v_m) = \frac{3\pi}{8} \frac{1-\frac{\nu_m}{2}}{1-\nu_m^2} \quad (5-12)$$

where F_θ is a term that takes into account orientation components (fracture orientation and stress loading direction) and p is the percolation parameter from Equation (2-3). For uniaxial compression conditions and uniformly distributed fracture pole orientation, F_θ is equal to $2/15$.

For the no-interaction case, still in frictionless conditions, the expression becomes:

$$E_{(no\ interaction)} = \frac{E_m}{1 + \frac{\frac{2}{\pi}F_\theta}{N(v_m)}p} \quad (5-13)$$

Both expressions are compared to the results from Figure 5-1 for the frictionless case and are shown in Figure 5-5.

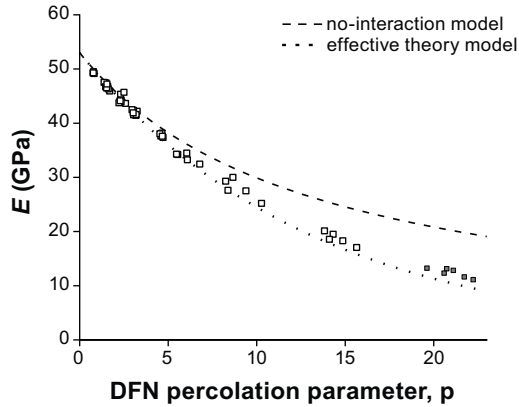


Figure 5-5. Evolution of the rock mass Modulus with increasing percolation parameter p . Comparison between the 3DEC numerical simulations (empty squares), the effective model from Equation (5-11) and the no-interaction model from Equation (5-13).

Case $k_m(l) \ll k_s$

In this case we can demonstrate that the effective modulus can be written as:

$$E_{eff} = \frac{k_s}{F_\theta \cdot P_{32} + k_s/E_0} \quad (5-14)$$

with P_{32} defined in Equation (2-2).

The expression is valid for both the no-interaction model and the effective theory.

General case

In the general case, the Young's modulus results from the contribution of small fractures, whose deformation is dominated by the deformation of the surrounding matrix, and large fractures, whose deformation is due to the stiffness and the friction on the fracture walls. The limit between both groups is the stiffness length $l_s = \frac{E_m}{k_s}$. If k_s depends on fracture size or normal stress, l_s varies accordingly.

For the no-interaction model, an approximate solution is:

$$\frac{1}{E_{(no\ interaction)}} = \frac{1}{E_m} + F_\theta \left(\frac{P_{32}(l > l_s)}{k_s} + \frac{2}{\pi} \frac{p(l < l_s)}{N(v_m)E_m} \right) \quad (5-15)$$

where $p(l < l_s)$ is the percolation parameter for fractures smaller than l_s ; $P_{32}(l > l_s)$ is the fracture density for fractures larger than l_s .

More elaborate expressions are derived for the effective theory in Davy et al. (2018) but the results are qualitatively similar to the Equation (5-15). In most of the cases, the predictions yield a good match with the numerical solution.

Consequence for a multi-scale DFN

Geological fractures are complex, ubiquitous, and observable at all scales (Tchalenko 1970), which poses the issue of the scales that control the fracture network properties. As a geologically relevant case, we develop the expressions for power-law fracture size distributions. In addition to being geologically relevant, power laws are the only functions that have no characteristic scale, except their lower and upper bounds l_{min} and l_{max} , respectively.

According to Equation (5-15), calculating the effective modulus amounts to evaluating both the density parameter $P_{32}(l > l_s)$ and the oriented percolation parameter $p(l < l_s)$. In the case of a power-law size distribution, both expressions result from the integral of power-law functions with bounds $[l_s, l_{max}]$ for P_{32} , and $[l_{min}, l_s]$ for p . The integrals are dominated by one of their bounds, and the critical parameter to determine which bound dominates is the exponent of the power-law functions. Since P_{32} is the second moment of the size distribution (i.e., the surface), and p the third moment (i.e., the volume surrounding the fractures), both expressions have different behaviours according to the size exponent a_{3d} :

- If $a_{3d} < 3$, both P_{32} and p are dominated by the upper bound, i.e., l_{max} and l_s , respectively. In the general case where $l_{max} \gg l_s$, P_{32} is the dominant term and the Young's modulus is dominated by the largest "frictional" fractures.
- If $a_{3d} > 4$, both P_{32} and p are dominated by the lower bound, i.e., l_s and l_{min} , respectively. In the general case where $l_{min} \ll l_s$, p is the dominant term and the Young's modulus is dominated by the smallest "frictionless" fractures.
- If $3 < a_{3d} < 4$ P_{32} is dominated by its lower bound l_s , and p by its upper bound l_s . The Young's modulus is controlled by the fractures whose size is around l_s .

Because the exponents measured from field mapping are generally between 3 and 4, the hypothesis that the fractures of size l_s – i.e., in the range of 1–50 m for hard rock geology – are the most important for elasticity appears very likely.

We refer to Section 7.4 for an application to the Forsmark case.

Contributions from fracture normal and shear displacement

The contributions of fracture normal and shear displacements to the rock mass elastic parameters, as defined in Equation (4-4) and Equation (4-11), are varying with the normal and shear stiffnesses k_n and k_s , respectively. To estimate their relative contributions, we calculate the Young's modulus and Poisson's ratio in both ways, firstly by taking both normal and shear components ($E(k_s, k_n)$ and $\nu(k_s, k_n)$) and secondly by taking only shear ($E(k_s)$ and $\nu(k_s)$). The contribution of the normal displacement is then calculated as the difference between both expressions normalized by one of them: $C_n(E) = (E(k_s) - E(k_s, k_n))/E(k_s)$ and $C_n(\nu) = (\nu(k_s) - \nu(k_s, k_n))/\nu(k_s)$, for the Young's modulus and Poisson's ratio, respectively.

Figure 5-6 shows $C_n(E)$ and $C_n(\nu)$ calculated by using the effective-medium approximation as a function of the ratio $x = k_n/(k_s + k_m)$ for different fracture densities and k_s values. Both $C_n(E)$ and $C_n(\nu)$ vary inversely with x which can be represented by $C_n(E) = 1/3x$ and $C_n(\nu) = 1/2x$, respectively.

A ratio of 100 between k_n and k_s gives a contribution of normal displacements of 0.3–0.5 % for the largest fractures (for which $k_s \gg k_m$) and even less for the smaller ones. This justifies neglecting normal displacements in the deformation for most of the cases reported in the literature.

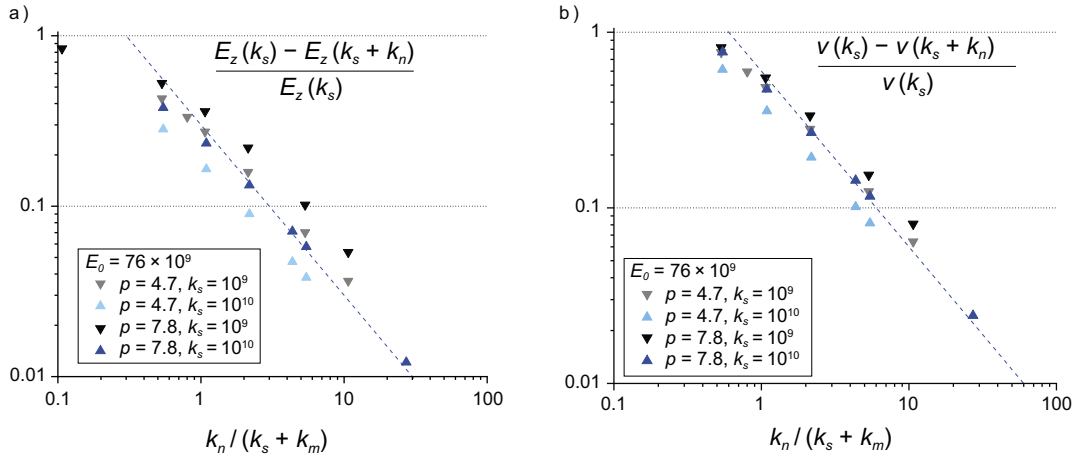


Figure 5-6. Figure from Davy et al. (2018). Contributions of the normal displacements to a) Young's modulus and b) Poisson's ratio as a function of the ratio $k_n/(k_s + k_m)$. k_s and E_0 units are in (Pa) in the figure caption. In both plots the y axis represents a normalized value of the Young's Modulus and Poisson's ratio sensitivity to the ratio $k_n/(k_s + k_m)$, expressed as the variation between estimates derived from conditions where only the shear displacements are accounted for (noted $E_z(k_s)$ and $\nu(k_s)$) and conditions where both normal and shear displacements are accounted for (noted $E_z(k_s + k_n)$ and $\nu(k_s + k_n)$), normalized by the "shear displacement only" condition (i.e. $E_z(k_s)$ and $\nu(k_s)$).

5.3.4 Comparison with other approaches – empirical methods for rock mass classification

Let's recall the context presented in Selroos et al. (2021): "The way the fractures of the rock are considered to derive the rock mass properties has indeed evolved significantly since the first rock mass quality index, the Rock Mass Quality Designation (RQD) introduced by Deere (1963) which preceded the Q system (Barton et al. 1974), the RMR (Bieniawski 1973) and the GSI with the associated Hoek-Brown constitutive model for rock mass strength envelope (Hoek and Brown 1997, 2019, Hoek et al. 2013). These empirical methods (see Appendix) were developed for use in civil and mining engineering in response to the need for ways to "rank" a specific rock mass, based on large part upon the fractures and their weakening and softening effects on the rock (Mas Ivars et al. 2011), before the rise of the Distinct Element Method (DEM) numerical modelling and of conceptualization of multi-scale natural fracture systems. These indicators are defined by a combination of simplified fracture system geometry (e.g. fracture frequency) and fracture surface "conditions" (e.g., roughness, quality from fresh to weathered, altered). The fracture system is seen as an assembly of blocks rather than as a network of discrete fractures. In addition, RMC systems are based on empirical relations which relate directly available observations – from core log or on outcrop cell mapping data – to indicative rock mass modulus and strength envelope. Hence the true nature of the fracture system is reduced to local and available observations, assuming that an indicative apparent fracture frequency and number of fracture sets (main orientations) are sufficient to constrain the impact of the fractures on the rock mass modulus and strength.

Even though RMC systems and relations are in widespread use in engineering design, where they appear as fast and well suited for standard construction and design purposes (Staub et al. 2002), their scope of use is becoming narrower (Hoek et al. 2013). Their limited accuracy is increasingly questioned (Pells et al. 2017) and their inability to consider strength anisotropy (resulting from a preferred fracture orientation), scale effect (resulting mainly from the combined effect of fracture intensity and fracture size), and strain softening/weakening is a strong drawback (Mas Ivars et al. 2011). This is even more so for the fracturing conditions prevailing in the Fracture Domains at Forsmark, where the fracture system is rather sparse as compared to the standard conditions for which the GSI systems were originally developed (Hoek et al. 2013).

5.3.5 Comparison with other approaches – DFN approach

The work by Oda (Oda 1988; Oda et al. 1993) differs from the present approach by several assumptions.

Oda (1988) neglected the surrounding deformation of the elastic matrix (k_m term in Equation (4-10)). Davy et al. (2018) have shown that this assumption is only valid for fractures whose size is larger than the ratio $\frac{E}{k_s}$, which has been estimated to be a few meters.

Oda (1988) assumed that both the normal and shear stiffnesses decrease inversely proportional to the fracture size, i.e. $k_n, k_s \sim l^{-1}$. This leads to two remarks:

- For this special case where the ratio $\frac{E}{k_s}$ is proportional to the fracture size, the contribution of the fractures to deformation is the same as for frictionless fractures (Davy et al. 2018). The ratio between both resistances described in the step-1 section (τ_f and τ_m) is independent of the fracture size l . For any other relationship between k_n, k_s and l , τ_f/τ_m varies with l .
- In principle, the expressions of Oda (1988) can be extended to any kind of stiffness-size relationship, but this requires an in-depth rewriting of the expressions to correctly average the parameters of the different fractures (see the discussion in the next paragraph, Equation (5-16) and (5-17)). The expressions derived by Davy et al. (2018) are valid for any value of k_n, k_s .

Equation (5-5) is the general expression to average the fracture properties and to evaluate the contribution of the fracture network to the total deformation. The final expression leads to a tensorial expression of the compliance tensor (Equation (5-6)). To emphasize the differences between Oda (1988) and Davy et al. (2018), we simplify Equation (5-5) and (5-6) to make it a simple algebraic relationship, i.e. not in its tensorial form. For Davy et al. (2018), the expression is written as:

$$\frac{1}{E_{eff}} = \frac{1}{E} + \frac{1}{V} \sum_f \frac{S}{k_s + E/l} \quad (5-16)$$

For Oda (1988), it is written as:

$$\frac{1}{E_{eff}} = \frac{1}{E} + \frac{1}{V} \frac{\sum_f S.l}{\sum_f \frac{k_s}{l}} \quad (5-17)$$

Both expressions are clearly different even for a set of fractures with constant size and large k_s (i.e., if $k_s \gg E/l$). In this case, the correct expression (Equation (5-16)) leads to the harmonic sum of the fracture stiffnesses while Oda (1988) writes the fracture compliance as the inverse of the arithmetic sum of k_s . The problem is even more important if the fractures have a broad distribution of sizes and orientations. On the other hand, the tensorial aspect of the compliance matrix is consistent for both approaches apart from the averaging issue.

At last, Davy et al. (2018) developed the expression of the effective elastic properties by considering the interactions between fractures. The result is a significant softening of the effective elastic modulus, especially when the shear stiffnesses k_s are small. This is not considered in Oda (1988).

6 Stress fluctuations

6.1 Origin of stress fluctuations

We define stress fluctuations as any local change in the stress tensor relative to the remote reference value. These variations are induced by the presence of heterogeneities (the fractures in our case) with mechanical properties different from the surrounding rock. The normal and shear displacements on each fracture cause a stress disorder with a stress concentration at the tips and a stress shield above and below the central part (Jaeger et al. 2007). The extent of the perturbations depends on the fracture geometrical and mechanical properties. At a DFN scale, a fracture perturbation potentially affects the stress loading conditions of the surrounding fractures and makes spatial distribution of the stress field even more complex. The fluctuations, in Figure 6-1, show both variations of orientation and magnitude of the principal stresses. Qualitatively, we see that the correlation length of the fluctuations is likely shorter for the case DFN *n03* and the induced disruption is more intense for DFN *n08*.

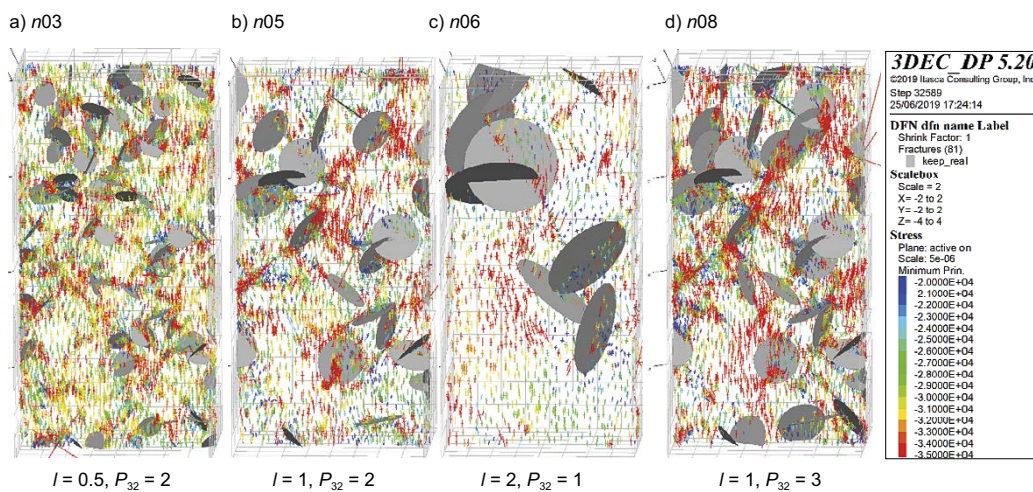


Figure 6-1. Representation of 2D vertical cut views (plane $y = 0$) from 3D SRM specimen of dimensions 4 by 4 by 8 meters. The fractures intersected by the visualization plane are represented in grey. Local stresses are represented with lines colored, oriented and scaled according to the principal stresses. The color scale refers to the maximum principal stress, expressed in the 3DEC convention of negative compressive stress in the figure caption (negative values of the “Minimum Prin.” stress refer to the maximum principal stress in absolute value). In the example $k_s \equiv 0$ and the DFN models (Table 2-1) are a) *n03* b) *n05*, c) *n06* and d) *n08*. The SRM specimens are loaded by a vertical maximum principal stress $\sigma_1 = 3 \times 10^{-2}$ MPa.

6.2 Stress fluctuation indicators

6.2.1 Scale

Stresses can be computed at different scales (Figure 6-2) and locations in the SRM specimen. The finest resolution scale is that of zones (volumetric meshes) in the model since stress is defined from the zones in the numerical model. The coarsest resolution scale is the specimen model itself, onto which boundary conditions are applied. In between, stresses are evaluated over intermediate length scales – by varying the diameter of sampling stress measurement spheres. The measurement spheres can be uniformly distributed through the SRM sample (Figure 6-3) or centered around the fractures (Figure 6-4). The stress for each measurement sphere is computed as the mean of stresses measured in the zones located at the sphere surface.

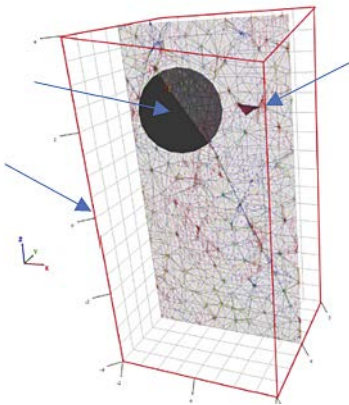


Figure 6-2. Illustration of the typical length scales. The SRM sample dimensions (red line), one fracture (grey) and one zone are outlined (dark red).

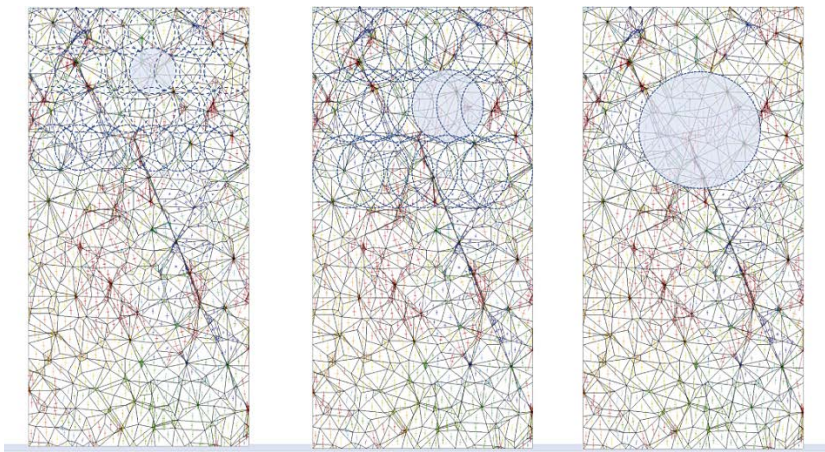


Figure 6-3. 2D schematic view of measurement spheres in a SRM specimen. From left to right the measurement scale is increased (all measurements are done in 3D, i.e., on spheres). Stress tensors are computed over spheres (outlined as blue dashed circles) evenly distributed all over the SRM samples (not centered around fractures). The sampling process is repeated for various scales (increasing measurement sphere diameter, from left to right).

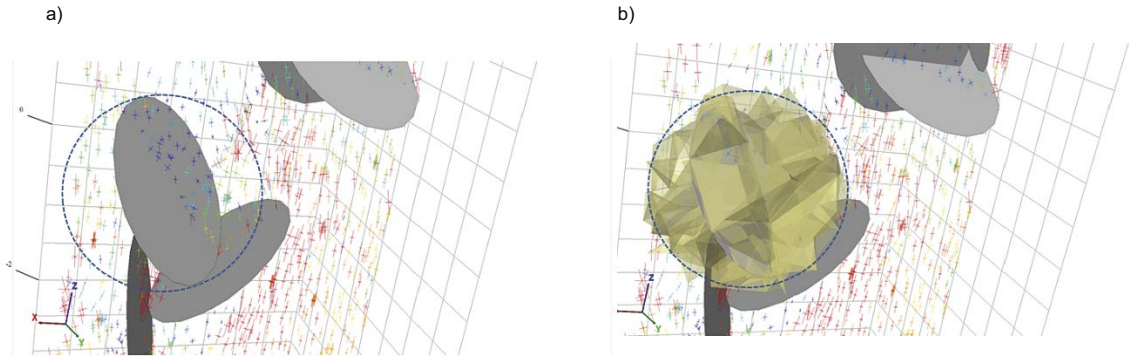


Figure 6-4. Definition of the spherical volume around a fracture onto which the stress field is averaged. a) sketch of the measurement sphere and b) selection of the group of zones defined by the measurement sphere.

6.2.2 Scalar indicators

A first possibility to indirectly highlight stress fluctuations in a rock mass specimen is to compute fracture average displacements and to compare them with the predictions based on remote stresses (Equation (4-11)). More generally, from any set of stress tensor values, we consider several indicators:

- Around a fracture, the ratio between remote and local stress, expressed as a full tensor or as the shear stress component for an orientation equal to the fracture orientation.
- The components of the average stress tensor $\langle \sigma_{ij} \rangle$, with N the number of stress tensor values:

$$\langle \sigma_{ij} \rangle = \frac{1}{N} \sum_{n=1}^N \sigma_{ij,n} \quad (6-1)$$

- The probability density function (distribution) of scalar elements of the stress tensor, either a specific component (e.g., a directional component like σ_{zz} or the principal stress like σ_1) or a scalar invariant of the tensor (e.g., the Von Mises stress, Equation (6-2)).

The Von Mises stress, σ_e , emphasizes stress concentration and yielding potential of the rock mass. It can be expressed as a function of principal stresses ($\sigma_1, \sigma_2, \sigma_3$) or general stresses ($\sigma_{11}, \sigma_{22}, \sigma_{33}, \sigma_{12}, \sigma_{23}, \sigma_{31}$) as given below:

$$\sigma_e = \sqrt{\frac{1}{2}((\sigma_1 - \sigma_2)^2 + (\sigma_1 - \sigma_3)^2 + (\sigma_2 - \sigma_3)^2)}$$

$$\sigma_e = \sqrt{3J_2} \quad (6-2)$$

$$J_2 = \frac{1}{6}[(\sigma_{11} - \sigma_{22})^2 + (\sigma_{22} - \sigma_{33})^2 + (\sigma_{33} - \sigma_{22})^2] + \sigma_{12}^2 + \sigma_{23}^2 + \sigma_{31}^2$$

Where σ_{11}, σ_{22} and σ_{33} are the diagonal components of the stress tensor and σ_{12}, σ_{23} and σ_{31} are the shear stress components.

- A tensorial description (see next section) of the stress variability from Gao and Harrison (2016a, 2018a, b), followed by a scalar evaluation with the effective variance or dispersion term.

When applied to the SRM specimen, these indicators are adapted to account for the volumetric variations of the elementary zones into which stress tensors are evaluated. These variations result from meshing constraints associated with the presence of DFN. The contribution of each element is thus weighted by its volume in the computation of means and variability terms:

$$s_{ij} = \frac{1}{V} \cdot \frac{1}{N} \sum_{n=1}^N v_n \cdot s_{ij,n} \quad (6-3)$$

where i and j the stress tensor component indexes, n the index of the N zones of the sample, v_n the volume of zone n , s_{ij} the stress tensor components and V the volume of the given sample.

6.2.3 Tensorial indicators

Fully tensorial approaches for mathematically characterizing the variations of stresses have been recently evaluated by Gao and Harrison (2016a, b, 2017, 2018b). Following their work, we recall below several tensor-based indicators which will be next used to characterize the stress fluctuations in the SRM specimen. As already used above in Equation (6-3), the tensorial approach for deriving an average stress tensor from a set of local values – the Euclidian mean stress tensor $\bar{\mathbf{S}}_E$ – is defined as:

$$\bar{\mathbf{S}}_E = \frac{1}{V} \sum_{i=1}^n \mathbf{S}_i v_i \quad (6-4)$$

where S_i is the stress tensor of the i th zone, v_i is the volume of this zone, n is the number of zones and V is the volume of the sample.

The Euclidian dispersion D_E of the stress tensors S_i is:

$$D_E = \sqrt{\frac{1}{V} \sum_{i=1}^n \|\mathbf{S}_i - \bar{\mathbf{S}}_E\|_F^2 v_i}$$

with

$$\|\mathbf{S}_i - \bar{\mathbf{S}}_E\|_F^2 = \text{tr}((\mathbf{S}_i - \bar{\mathbf{S}}_E)(\mathbf{S}_i - \bar{\mathbf{S}}_E)^T) \quad (6-5)$$

For more clarity we define $T_i = S_i - \bar{S}_E$ and develop the previous expression as:

$$\|\mathbf{S}_i - \bar{\mathbf{S}}_E\|_F^2 = \|\mathbf{T}_i\|_F^2 = T_{xx_i}^2 + T_{yy_i}^2 + T_{zz_i}^2 + 2T_{xy_i}^2 + 2T_{xz_i}^2 + 2T_{yz_i}^2$$

For the calculation of generalized variance and effective variance, we define the vector s_{di} using a half-vectorization function of the tensor S_i by stacking together only the upper triangle columns of the tensor into a column vector containing the distinct components. In the same way, the half vectorization of the mean tensor \bar{S}_E is defined.

$$\mathbf{s}_{di} = \text{vech}(\mathbf{S}_i) = [\sigma_{x_i} \ \tau_{xy_i} \ \tau_{xz_i} \ \sigma_{y_i} \ \tau_{yz_i} \ \sigma_{z_i}] \quad (6-6)$$

$$\bar{\mathbf{s}}_d = \text{vech}(\bar{\mathbf{S}}_E) = [\bar{\sigma}_x \ \bar{\tau}_{xy} \ \bar{\tau}_{xz} \ \bar{\sigma}_y \ \bar{\tau}_{yz} \ \bar{\sigma}_z]$$

The covariance matrix is calculated as

$$\Omega = \frac{1}{V} \sum_{i=1}^n (\mathbf{s}_{di} - \bar{\mathbf{s}}_d) \cdot (\mathbf{s}_{di} - \bar{\mathbf{s}}_d)^T v_i \quad (6-7)$$

Based on the covariance matrix, the generalized variance and effective variance are respectively given by:

$$V_{g|d} = |\Omega|$$

$$V_{e|d} = \frac{1}{2^{p(p+1)}} \sqrt{|\Omega|} \quad (6-8)$$

where $|\cdot|$ denotes the matrix determinant and p is the dimension of the stress tensor ($p = 2,3$).

The transformational invariance of the Euclidian dispersion, generalized variance and effective variance associated to the distinct tensor components was demonstrated in Gao and Harrison (2018b), i.e., their values are independent of the coordinate system. The Euclidian dispersion (D_E) and square root of the effective variance $\sqrt{V_{e|d}}$, both having “stress” unit, will be used as stress fluctuation indicators.

6.3 Results

6.3.1 Exploratory study – isolated fracture

At the coarsest resolution scale (SRM specimen dimensions), there is only one stress state directly deduced from the imposed boundary conditions. For simplicity, this limit is called remote stress. This is defined such that the maximum principal stress σ_1 is vertical and the intermediate and maximum principal stresses, σ_2 and σ_3 are horizontal and equal to σ_c . If no fracture is embedded in the SRM specimen, with a uniform and isotropic intact rock, the stress state is constant all over the sample.

When a fracture is added to the specimen, the displacement of the fracture plane induces stress fluctuations. This is illustrated in Figure 6-5. The Von Mises (VM) stress measured far from the fracture is $(\sigma_1 - \sigma_c)$, the value for a homogenous rock submitted to the abovementioned stress conditions (the initial stress condition is represented by the green color in the figure). The VM stress increases around the fracture tip and decreases above and below the central part of the fracture (known as shielding effect). For isolated fractures with no friction in an isotropic matrix, analytical solutions exist (Fabrikant 1999). The VM stress probability density function (pdf) resulting from the isolated fracture configuration is plotted in and b). The distribution is dominated by the central part around the remote stress (hatched zone) value which reflects the limited volume of influence around the fractures. The values to the left of the central part reflect the shielding effect around the fracture while those to the right reflect the stress increase at the fracture tips.

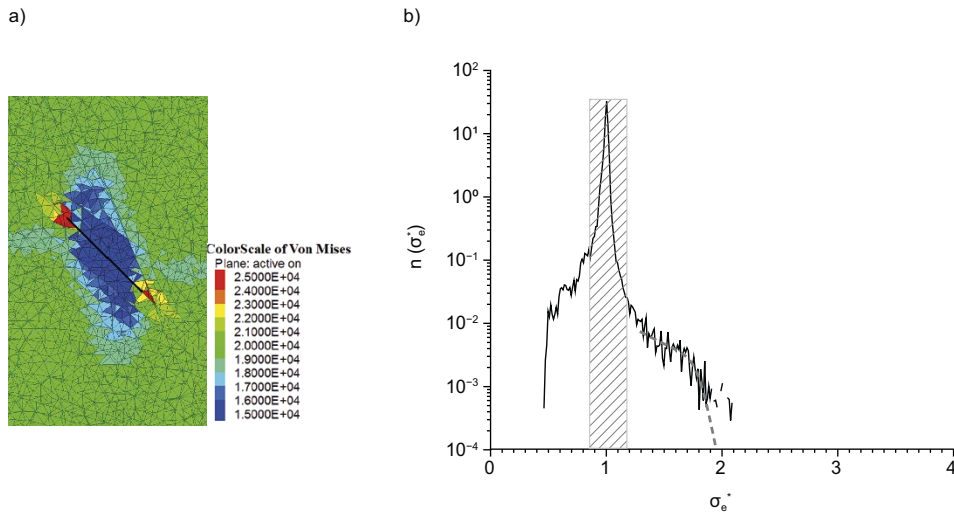


Figure 6-5. Stress distribution in a SRM specimen containing one isolated fracture. a) 2D vertical cut view of a SRM with only one fracture (fracture trace in black), loaded vertically by $\sigma_1 = 3 \times 10^{-2}$ MPa and laterally by $\sigma_2 = \sigma_3 = 1 \times 10^{-2}$ MPa, resulting in a Von Mises Stress $\sigma_e = 2 \times 10^{-2}$ MPa far from the volume of influence of the fracture and b) Pdf of the normalized Von Mises stress $n(\sigma_e^*)$.

6.3.2 Exploratory study – DFN scale

At DFN scale, we study the global distribution of local stress variations due to an assembly of fractures. The analysis is based on the $n01$ to $n12$ DFN models with 10 realizations by model. The stress spatial distribution (vertical stress component σ_{zz}) resulting from the loading with σ_1 in the vertical direction, are illustrated in Figure 6-6 for two of the DFN models. In the case of low fracture density and short fractures (model $n01$), most of the zones in the model are only slightly disturbed by the presence of fractures (σ_{zz} remains close to σ_1 which is vertical), while in the case of a higher density and especially larger fractures (Figure 6-6b), the vertical stress component is significantly disturbed with almost no zones having the same values as the remote stress σ_1 .

The density distributions of the normalized Von Mises stress component ($\sigma_e^* = \sigma_e / (\sigma_1 - \sigma_c)$), are plotted in Figure 6-7. The peak value at $\sigma_e^* = 1$ reflects the non-disturbed stress state when the DFN density is low. When the amount of fractures increases, the dispersion around the peak significantly increases and tends to become asymmetric, with an increase of the distribution tailing towards large values. The distribution $n(\sigma_e)$ results from the superposition of stresses at locations not affected by the DFN and at locations affected by the fractures. So, when the amount of fractures in the specimen increases, the proportion of disturbed zones increases, and the tails of the distributions become broader. The semi-log plot in Figure 6-7b emphasizes an exponential decay towards large σ_e^* values.

We next compare the relative variations of the low and high tails of the distributions when the amount of fracture increases. If interactions between fractures can be neglected, the differences between the distributions should be explained by a change of the affected volume only. To do this, we define a new normalized distribution $[n(\sigma_e^*)]^*$ as:

$$[n(\sigma_e^*)]^* = n(\sigma_e^*) \cdot \frac{V}{\sum l^3} \quad (6-9)$$

The normalization volume of $[n(\tau_e)]^*$ is thus proportional to the volume occupied by the DFN (defined as the sum, over all fractures of size l , of the volume l^3). The results are plotted in Figure 6-8. When comparing Figure 6-8 to Figure 6-7b, we observe that with the second normalization, the shielding-type part of the distributions (values below 1) held each other on a single trend, whereas the stress amplification-type part still differs from one DFN model to the other. For $\sigma_e^* > 2$, all the distributions tend to display an exponential decay (dashed lines in Figure 6-8), whose rate parameter k (defined in Equation (6-10)) is constant for all the models but $n12$, for which the decay is less sharp.

$$n(\sigma_e^*) \sim \exp(-k \cdot \sigma_e^*) \text{ for } \sigma_e^* > 2 \quad (6-10)$$

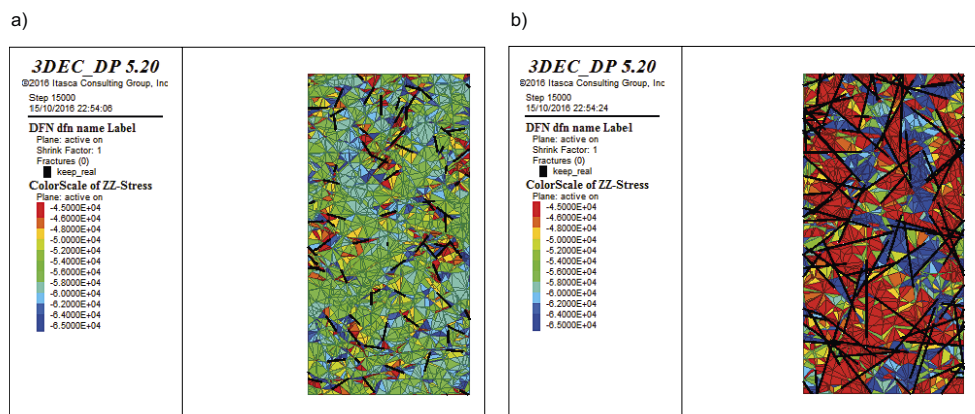


Figure 6-6. 2D vertical cut view of the stress vertical component σ_{zz} for a) $n01$ and b) $n12$ models. The DFN traces are plotted in black. Note that the legend is written with the 3DEC convention of negative compressive stresses.

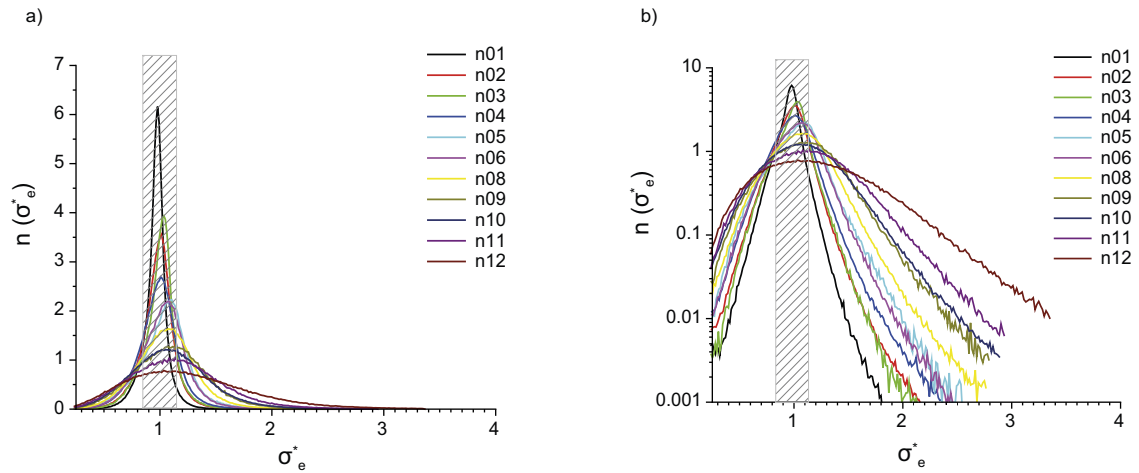


Figure 6-7. Probability density function $n(\sigma_e)$ of the n01 to n12 models. a) Linear plot and b) semi-log plot. The grey hatched zone reflects Von Mises values equivalent to the remote stress conditions, by analogy with Figure 6-5.

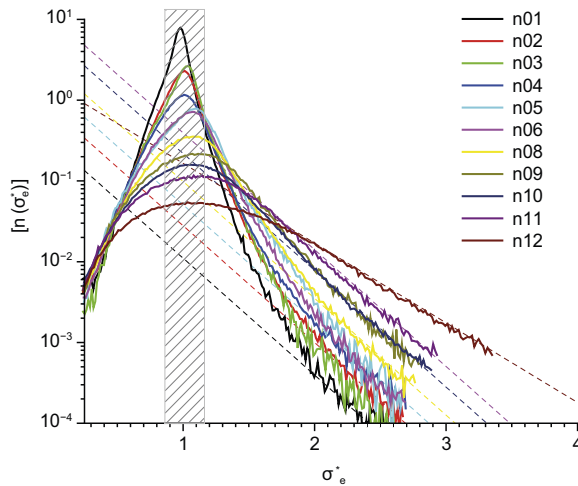


Figure 6-8. Probability density functions $[n(\sigma_e^*)]^*$ of the n01 to n12 models.

6.3.3 Exploratory study – fracture vicinity

We also study how the environment of a fracture in a DFN affects the local stress field and the actual displacement around each fracture. Thus, for each fracture of each DFN we compute the average shear displacement (t) and the average shear stress (τ) applied at the fracture plane. The latter is calculated by projecting, on the fracture plane, the stress state inferred in a sphere centered at the fracture center and of radius equal to 1.5 times the fracture radius. Each average t and τ values are then normalized by the theoretical values corresponding to isolated fractures (i.e., same SRM specimen dimensions and remote stress condition). The normalization factor for τ is simply the shear component, in the orientation of the fracture plane, of the remote stress (noted τ_R). The normalization factor for the displacement (noted t_{th}) is given by Equation (4-11).

For fractures in a DFN, the surrounding fractures of any fracture in the network, whether or not they intersect, induce stress perturbations which will, in turn, change the local stresses around the fractures. The local consequences on the shear displacements in the fracture plane are illustrated in Figure 6-9.

Normalized average shear stresses and displacements are computed over all the fractures and DFN of the SRM specimen numerical loading experiments of the preceding sections, i.e., 10 realizations of the DFN models $n01$ to $n12$, with 3 different values of fracture shear stiffness k_s (0, 12 and 72 GPa/m). The results are presented in the Figure 6-10 and Figure 6-11.

The evolution of $\langle \tau / \tau_R \rangle$ with the DFN percolation parameter p is plotted in Figure 6-10a. If there is no significant perturbation in the stress field, then we expect $\langle \tau / \tau_R \rangle = 1$, so that each fracture of the DFN behaves as one isolated fracture directly loaded by the remote stress conditions. If the stress field perturbation is more significant, we expect a variation between the measured and the remote value, so that $\langle \tau / \tau_R \rangle$ would no longer be equal to 1. We observe that, if k_s is sufficiently large (case $k_s = 72$ GPa/m) the normalized stress ratio is indeed equal to 1. For lower values of k_s , we observe a tendency for the ratio to decrease when the DFN percolation parameter increases. The maximum variation of the ratio, observed over the range of the tested cases, is a 10 % decrease between the theoretical unperturbed case and the measurement. We interpret the downward trend as a prevalence of the fracture stress shielding effect with respect to the fracture tips stress concentration effects. The evolution with p of the shear displacement ratio t / t_{th} (Figure 6-10b), shows a clear increase with p especially for the frictionless case where it reaches a jump of 50 % for the largest values of p .

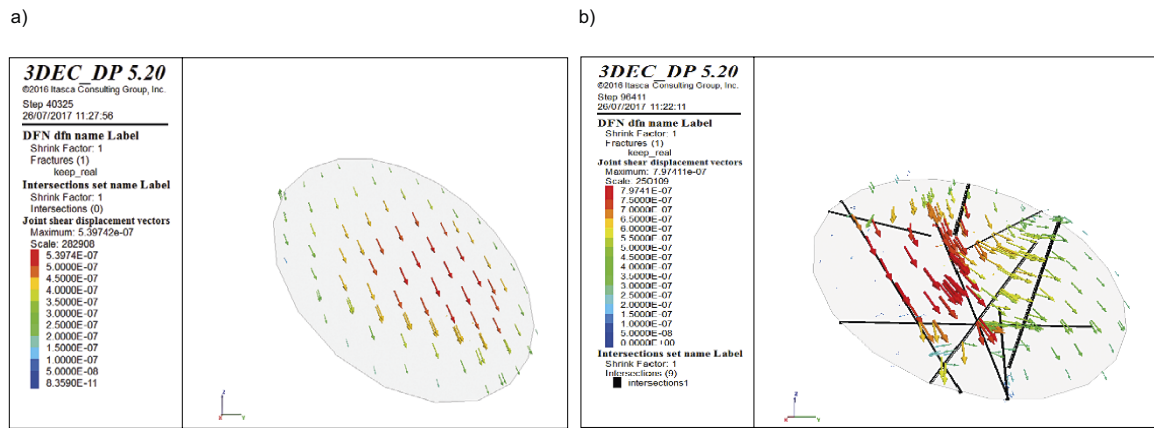


Figure 6-9. View of local shear displacement on a fracture. a) Isolated fracture and b) fracture surrounded by other fractures (intersection traces in black).

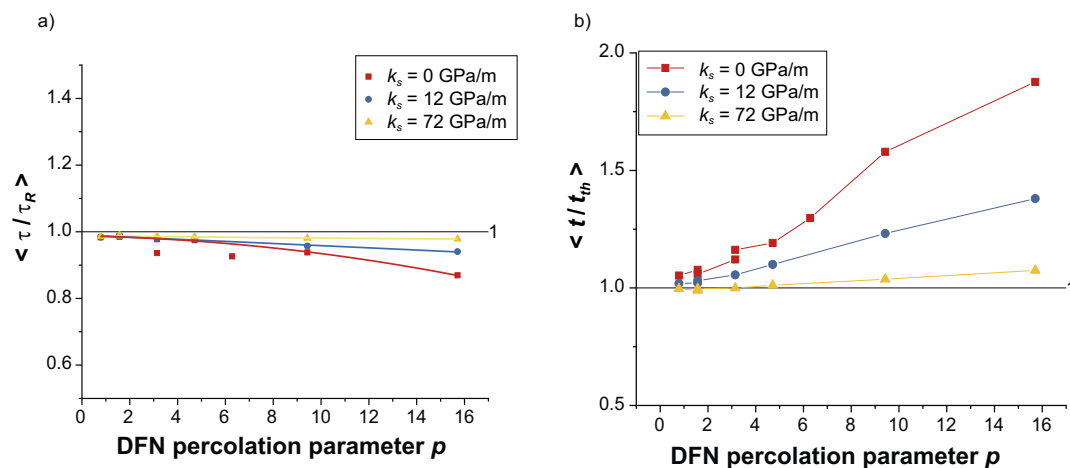


Figure 6-10. Evolution with the DFN percolation parameter p of a) τ / τ_R and b) t / t_{th} .

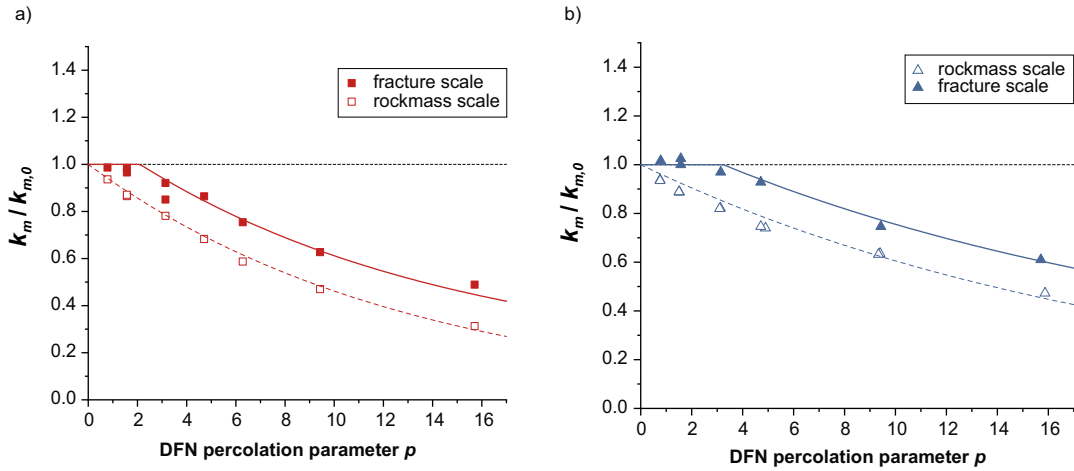


Figure 6-11. Evolution, with the DFN percolation parameter p , of the ratio $\langle k_m \rangle / k_{m,0}$ for the local matrix stiffness (filled symbols) and effective matrix stiffness (open symbols), for the case of a) frictionless fractures (equivalent to $k_s = 0$) and b) $k_s = 72 \text{ GPa/m}$.

Finally, the fracture shear stress and displacement measurements are used to back-calculate the matrix stiffness k_m which represent the effect of the surrounding fractures and therefore define a local effective matrix stiffness. In practice, for each fracture, a local matrix stiffness is calculated based on Equation (4-11) and expressed as follows:

$$k_{m,f} = \frac{\tau_f}{t_f} - k_{s,f} \quad (6-11)$$

where the subscript f refers to the fracture f .

For each DFN, the average local matrix stiffness $\langle k_m \rangle$ is computed by averaging over all the local values $k_{m,f}$ of the fractures of each DFN. We finally consider the evolution, with the DFN percolation parameter, of the ratio $\langle k_m \rangle / k_{m,0}$ (with $k_{m,0}$ the equivalent matrix stiffness for an isolated fracture, (Equation (4-10))). Its evolution is compared to the effective matrix stiffnesses estimated directly from the specimen scale measurements (results in Figure 5-1) and normalized by $k_{m,0}$. The results are plotted in Figure 6-11. The reference value $\langle k_m \rangle / k_{m,0} = 1$ simply denotes conditions for which the effect of the fractures on the effective matrix stiffness is negligible. The downward trend of $\langle k_m \rangle / k_{m,0}$ when increasing p denotes the softer and softer nature of the effective rock matrix.

We note that the evolution of the fracture scale estimates is similar to the evolution of the rock mass scale estimates, but with a clear shift towards larger percolations. For the low values of the percolation parameter (roughly below $p = 2.5$), where the fractures are locally surrounded by the intact rock the effect of surrounding fracture can be neglected, while globally at the rock mass scale the effective matrix stiffness is already affected to this presence or relatively isolated fractures. It is only for higher values of the percolation that each fracture locally behaves as in the effective rock matrix rather than as in the intact rock matrix. The gap between the local and the rock mass matrix stiffnesses is also related to the mechanical properties of the rock and the fractures (comparing Figure 6-11a and b).

This last observation has important implications when applying the DFN methodology for cases where part of a DFN is replaced by effective properties while the other part is kept discrete (i.e., explicit) in the numerical modelling, because of the abovementioned shift.

7 Applying the methodology to multiscale DFN

7.1 Discrete and effective representation for a DFN

When applying the methodology, one can decide to replace all the rock mass by a homogeneous effective matrix stiffness or to keep part of the discrete fractures explicitly in a model and to replace only partially the DFN by effective properties (all illustrated in Figure 7-1). In this section, we show how to use the methodology in practice to evaluate the effective properties from a general case (multiscale DFN) and what are the consequences, in term of scale effect and stress fluctuations, of replacing fully or partially a DFN by these effective properties.

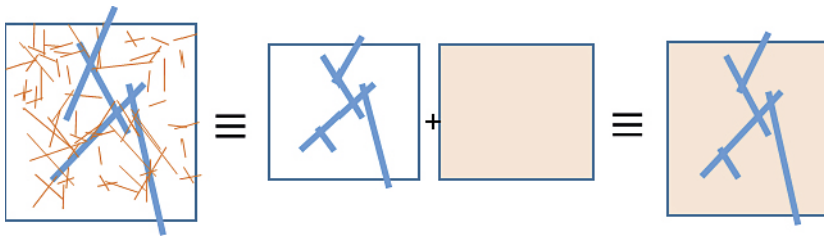


Figure 7-1. Schematic view of standard approaches for DFN models.

7.2 From DFN discrete to effective representation

7.2.1 Description of required input

The contribution of a population of fractures to the effective elastic properties at the boundaries of a rock specimen is computed with Equations (5-4), (5-5) and (5-10). The necessary input to infer the effective properties are:

- for each fracture, its size, surface, orientation and mechanical properties (mechanical model with normal and shear stiffnesses for elastic conditions and friction for critically stressed fractures (Equation (4-4) and (4-11)),
- the elastic properties of the rock into which the fractures are embedded,
- the volume of the fractured rock specimen, and
- the stress conditions applying at the boundaries of the rock specimen.

The proposed approach applies for conditions where the importance of the location of the fractures within the rock specimen is negligible when compared to the cumulated “population effect” of the DFN. Consequently, intersections between fractures also are neglected in the approach. The fractures are initially disc-shaped and are potentially cut by the rock specimen limits.

7.2.2 Description of the output

Equation (5-5) defines the components of the deformation tensor resulting from a stress state. It is used to compute all the components of the general compliance tensor, by successively applying small stress increments on the elements ($\sigma_{i,j}$) of the stress field initially given by the remote stress field. Depending on the conditions, the resulting effective properties may be isotropic or orthotropic and the compliance tensor is accordingly simplified.

7.2.3 Sensitivity to order

When using Equation (5-5) to cumulate, at the specimen scale, the deformations relative to all the individual fractures, the role of the order of insertion of the fractures may have some impact if interactions are considered (and the effective theory summarized in Equation (5-10) is applied). If the fractures that induce the most deformation are first added, then the iterative variation of effective modulus is significant from the outset, so that fractures added afterwards “see” a weaker effective medium, whereas, on the opposite “minor” fractures are first added, so that the significant one “see” a quasi-intact medium. This could occur when the fracture population is such that the distribution of fracture-deformation is wide, due to the nature of the fracture size distribution (e.g., the power-law model) or to the orientations.

The sensitivity to order of insertion is illustrated in Figure 7-2. A power-law DFN is defined (model from Section 7.4.1). We observe that the order of insertion has only a marginal effect of the final estimate of the elastic property.

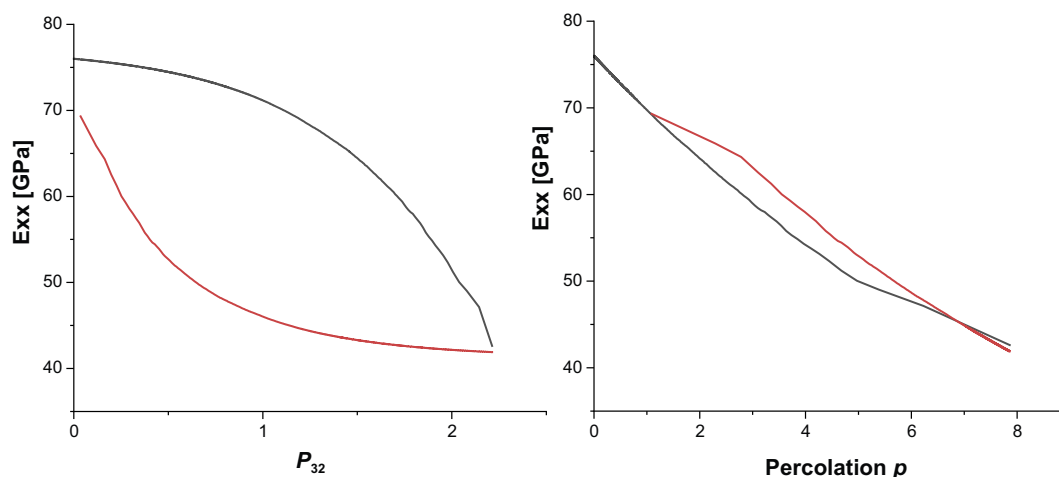


Figure 7-2. Test order sensitivity. Insertion order from the smallest to the largest fracture (black curve) and from the largest to the smallest (red curve).

7.3 Application to DFN with a power-law size distribution

7.3.1 DFN model and setup

We study the impact of changing the limit between explicit and effective fractures with the DFN model pl , whose parameters are provided in Table 2-1. The same density distribution model $n_{3D}(l)$ is used to define DFN realizations with fractures sizes distributed over the range $[0.4;4]$ and $[0.2;4]$. The density P_{32} of the first set is 4 m^{-1} and for the second set is 8.44 m^{-1} . The orientation distribution of the model is isotropic. One realization of each model is represented in Figure 7-3 and the corresponding density distributions of fracture sizes are given in Figure 7-4.

Two realizations of the model with $l_{min} = 0.4$ are generated (named *seed 1000* and *seed 3000*) and one realization of the model with $l_{min} = 0.2$ is generated (named *seed 1000*). The fracture mechanical parameters correspond to frictionless fractures and quasi-infinite normal stiffness. In these conditions the shear displacement over the fractures is maximized.

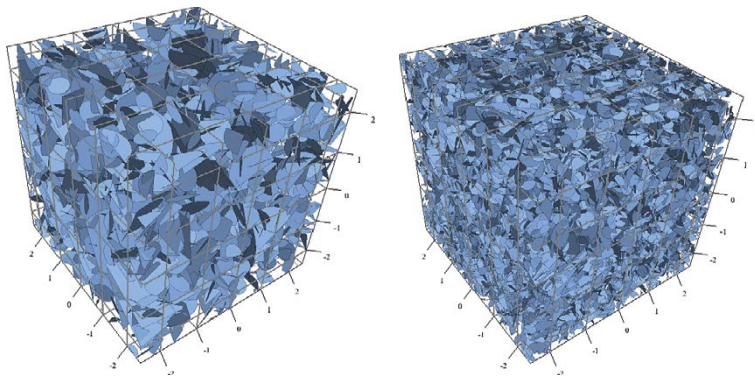


Figure 7-3. View of the DFN model with $l_{min} = 0.4\text{ m}$ (left) and $l_{min} = 0.2\text{ m}$ (right).

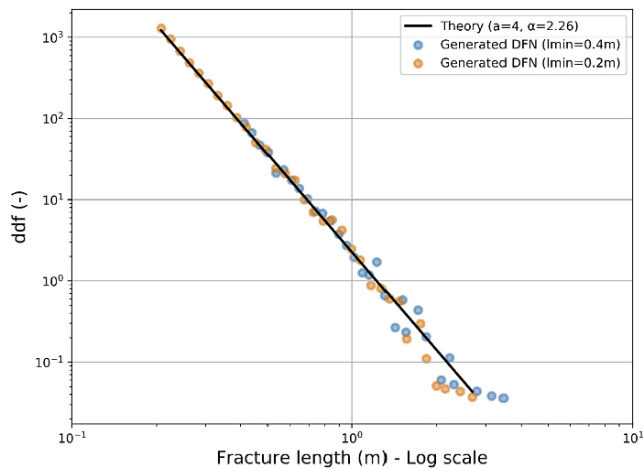


Figure 7-4. Density distribution of fracture sizes, $n_{3d}(l)$.

Some adaptations from the previously described numerical setup (Section 3) are done to deal with the specificity of the *pl* DFN models and the study of the effective/explicit representation:

- The specimen dimensions are changed from parallelepipedic to cubic with an edge length equal to 5 meters.
- A pre-processing is performed over each DFN realization to remove potential biases due to fractures intersecting the borders. The fractures intersecting the boundaries of the model (truncated disks) are replaced with equivalent disk fractures shifted inside of the sample until there are no intersection with boundaries.
- Filtering functions are written to divide each basic DFN in two parts, according a varying size limit (noted L_c), below which the contribution of the fractures to the effective elastic properties is determined, so that in further modelling, the intact rock is combined to this part of the DFN to define an effective rock matrix, and above which fractures are explicitly kept discrete in the numerical simulations.
- The effective compliance matrix of the sub-DFN below L_c is computed according to the relationship defined in Section 5 and following the workflow defined in Section 7.2.
- A numerical SRM specimen is built in 3DEC, based on the remaining discrete fractures and with effective elastic properties assigned in the zones.
- For each defined DFN realization, the limit L_c is increased from 0.8 m, 1.6 m and to 2 m. Each time the effective properties below L_c are computed and the 3DEC specimen accordingly built and tested.
- In the 3DEC numerical models, specific large fractures are identified, and their local displacement are systematically computed (when L_c varies), in addition to the SRM specimen scale macroscopic measures.
- Additional post-treatment functions are implemented to compute the stress fluctuations indicators listed in Section 6.2.
- The initial intact rock properties are $E_m = 76.9 \text{ GPa}$ and $\nu_m = 0.23$. The fracture mechanical properties are such that shear displacements are maximized (i.e., frictionless fractures) and the normal displacements are negligible (i.e., quasi-infinite normal stiffness k_n).

With this updated numerical setup, we systematically analyse the consequences of changing the size limit L_c . In Figure 7-5, we show the explicit part of the DFN for different values of L_c .

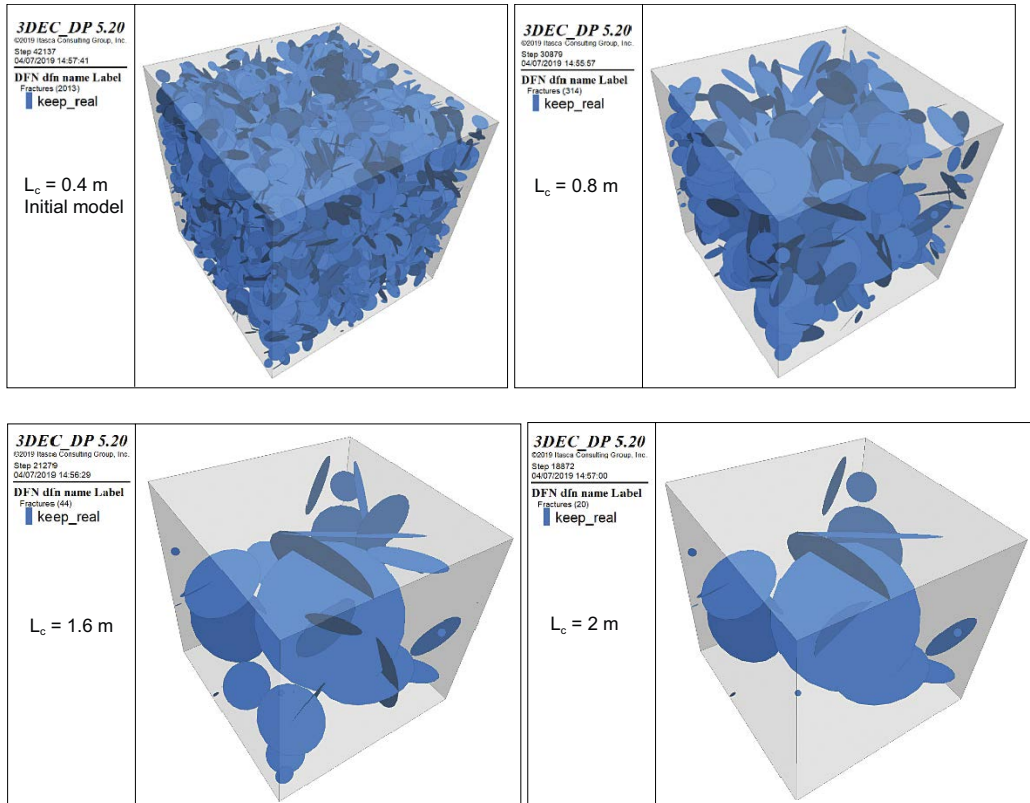


Figure 7-5. One DFN realization with several values of L_c .

7.3.2 Effective properties below L_c

The effective moduli, for the DFN made of fractures smaller than L_c , are given in Table 7-1 (for case $l_{min} = 0.4 \text{ m}$) and Table 7-2 (for case $l_{min} = 0.2 \text{ m}$).

Table 7-1. Effective properties for several values of L_c , case $l_{min} = 0.4 \text{ m}$.

L_c (m)	$E_{eff} (l < L_c)$ (GPa)	$\nu_{eff} (l < L_c)$ (-)	$\rho (l < L_c)$ (-)
$l_{min} = 0.4$ (intact rock)	76.9	0.23	0
0.8	65.1	0.27	2.0
1.6	56.5	0.30	3.85
2	53.9	0.30	4.43

Table 7-2. Effective Properties for several values of L_c , case $l_{min} = 0.2 \text{ m}$.

L_c (m)	$E_{eff} (l < L_c)$ (GPa)	$\nu_{eff} (l < L_c)$ (-)	$\rho (l < L_c)$ (-)
$l_{min} = 0.2$ (intact rock)	76.9	0.23	0
0.8	56.4	0.3	3.88
1.6	49	0.32	5.68
2	46.7	0.33	6.26

We check in Figure 7-6 that each particular DFN realization has an effective modulus which closely matches the expected average evolution with the percolation parameter (Equation (5-11) and (5-12)).

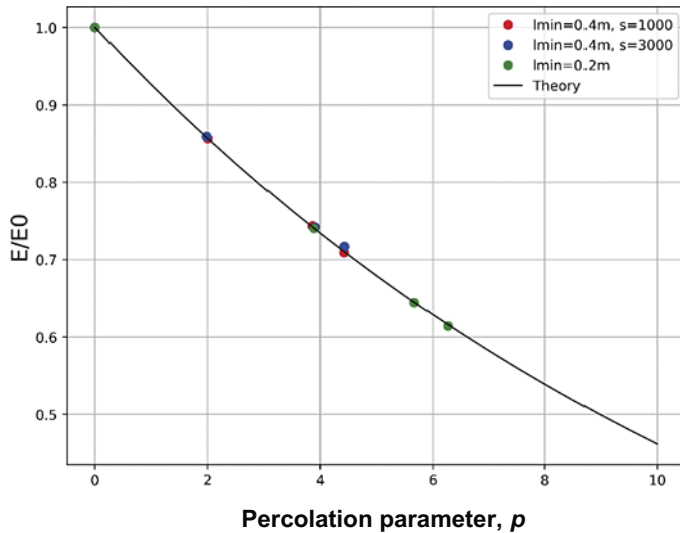


Figure 7-6. Evolution of the ratio $E_{eff} (l < L_c)/E_m$, between effective modulus of hidden fractures and modulus of intact rock with the DFN percolation parameter $p (l < L_c)$. The dots are computed from the particular DFN realizations and the curve is the analytical solution from Equation (5-11) and (5-12).

7.3.3 Rock mass macroscopic elastic properties

3DEC mechanical simulations are performed to compute the effective elastic properties of the SRM specimens defined with the different combinations of L_c coupled to the corresponding effective matrix properties (these models are called “global” models below, as a combination between effective matrix to account for the implicit fractures and explicit fractures). The results are plotted in Figure 7-7 and Figure 7-8. We see that regardless of the value of L_c , the final effective modulus and Poisson’s ratio are almost constant, thus confirming the capacity of the effective theory to define effective properties over a certain size range, even in the case of a power-law DFN. Nevertheless, we note some variations over the Poisson ratio estimates (15 %).

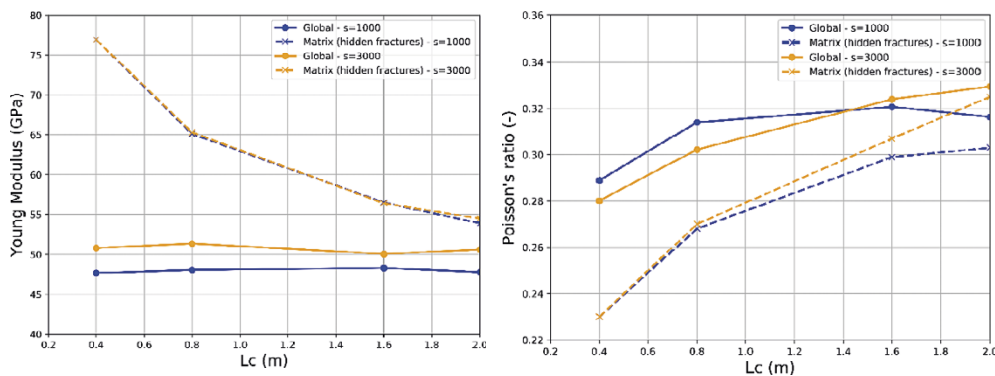


Figure 7-7. Evolution with L_c of the effective Young’s modulus and Poisson’s ratio, for the global models (effective matrix and explicit fractures) and the effective matrix (including implicit fractures, for two DFN realizations (blue and orange). Case $l_{min} = 0.4 m$.

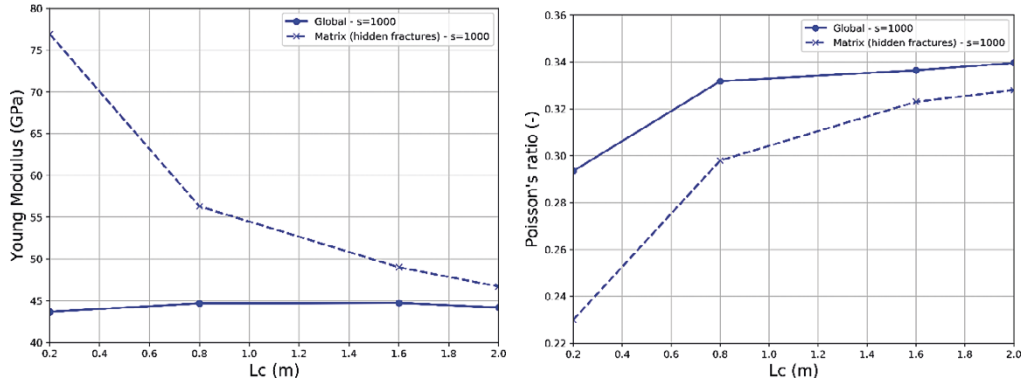


Figure 7-8. Values of effective Young's modulus and Poisson's ratio, for the global model and the effective matrix (including implicit fractures), for various values of L_c . Case $l_{min} = 0.2$ m.

7.3.4 Stress fluctuations

The results in this section are preliminary. We evaluate the sensitivity, in term of stress fluctuations in the SRM specimens, when the limit L_c is varied. The analyses are based on the same set of numerical simulations as in the previous section. We compute the evolution of the following indicators with L_c :

- Probability density function of the normalized Von Mises stresses in the zones $n(\sigma_e^*)$.
- Standard deviation of $n(\sigma_e^*)$, $sdev(\sigma_e^*)$.
- Stress Dispersion D_E (Equation (6-5)) and Square Root Effective Variance $\sqrt{V_{el}}$ (Equation (6-8)).

We first qualitatively visualize (Figure 7-9) the in situ stress tensors variations when L_c increases, on a vertical plane passing through the center of the model. We observe a first order spatial organization controlled by the largest fractures (case $L_c = 2$), which is still visible down to $L_c = 0.4$, although significantly altered by the explicit presence of more and more small fractures.

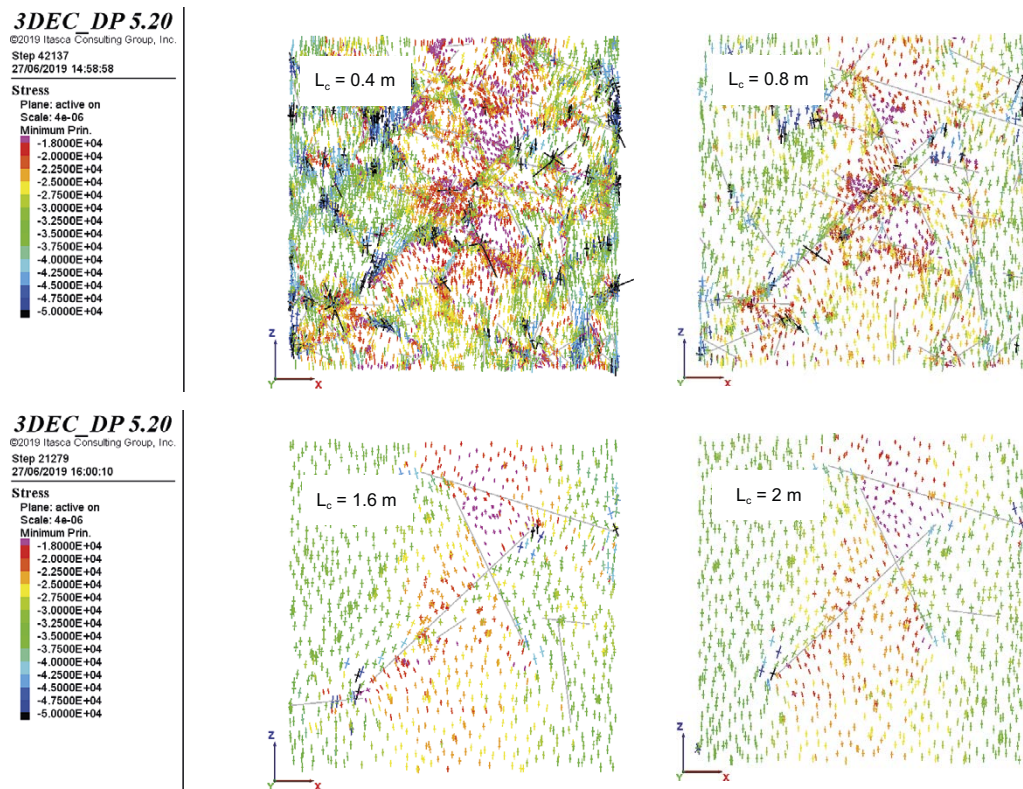


Figure 7-9. Stress tensor colored by maximum compressive stress, on a vertical cut plane (realization $s = 1000$) and oriented according to the principal stresses. Note that the legend is written with the 3DEC convention of negative compressive stresses.

Figure 7-10 and Figure 7-11 show a decrease of $sdev(\sigma_e^*)$ with increasing L_c , for the different cases studied. This trend is much the same for both realizations of the model with $l_{min} = 0.4$ and qualitatively similar to the results in Figure 6-7: increasing the percolation parameter of the explicit DFN tend to broaden the normalized Von Mises distribution. Thus, increasing L_c here tends to decrease the percolation level of the DFN part that remain explicit and to lower the spatial stress fluctuations. The same trend is observed for the case $l_{min} = 0.2$ with even more fluctuations when L_c is equal to 0.2 m (the explicit part of the DFN being the highest in this case).

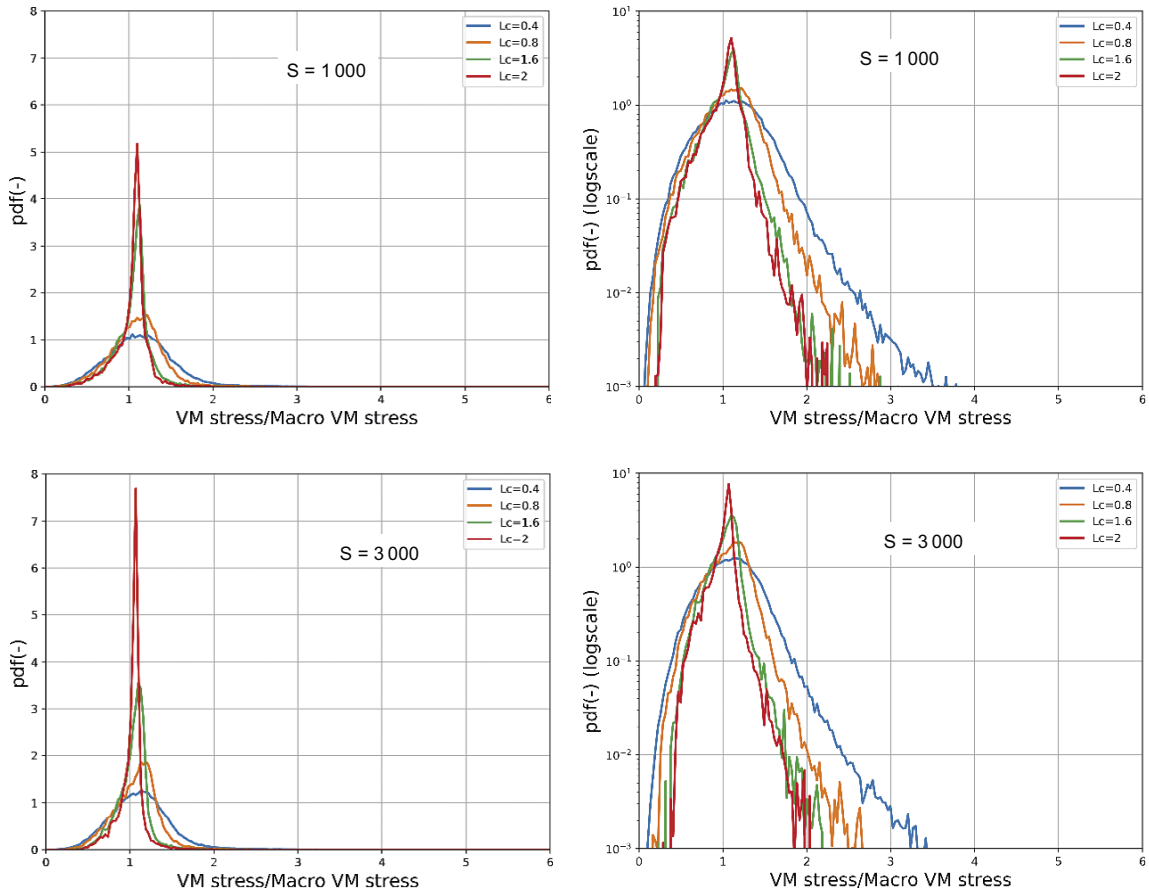


Figure 7-10. $n(\sigma_e^*)$ for the two DFN realizations with $l_{min} = 0.4$ m, linear scale (left) and log-lin scale (right).

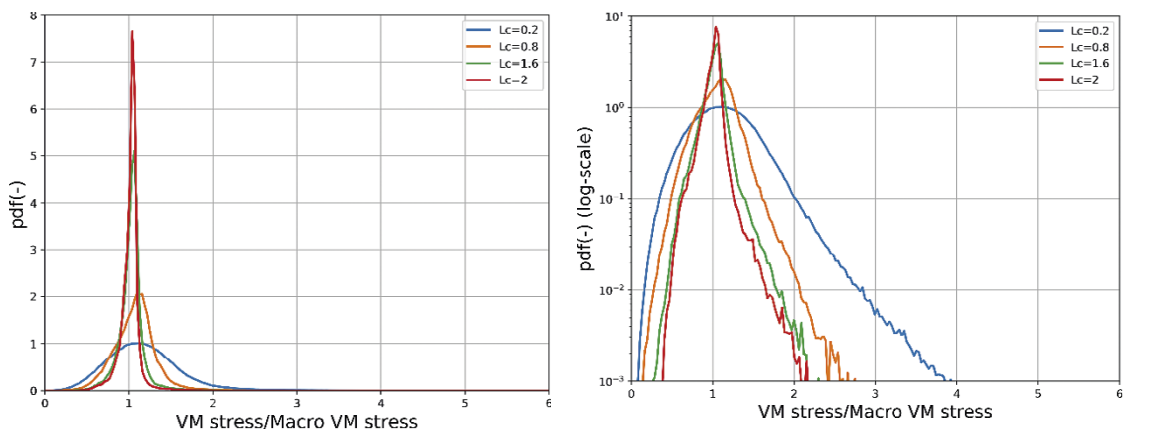


Figure 7-11. Probability density function of the normalized Von Mises stress, case $l_{min} = 0.2$ m, normal scale (left) and logscale (right).

The evolution, with L_c , of the stress variability indicators, the standard deviation $sdev(\sigma_e^*)$, the dispersion D_E and the square root of effective variance $\sqrt{V_{elid}}$ are plotted in Figure 7-12 and Figure 7-13.

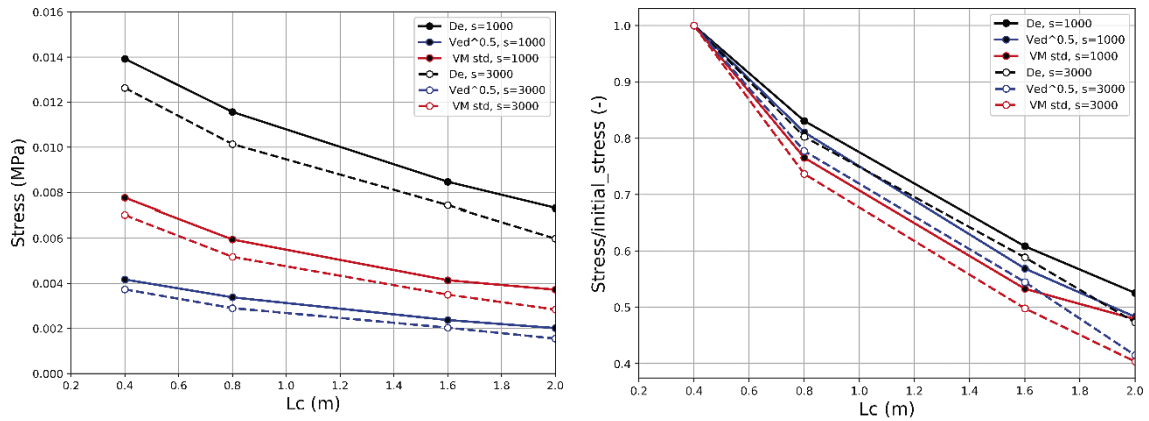


Figure 7-12. Evolution of the stress variability indicators with L_c for two DFN realizations with $l_{min} = 0.4$ m (solid lines and symbols for one, dotted lines and empty symbols for the other). (left) $sdev(\sigma_e^*)$ (in red), D_e (in black) and $\sqrt{V_{elid}}$ (in blue). (right) Same convention and values normalized by the values at $L_c = 0.4$ m.

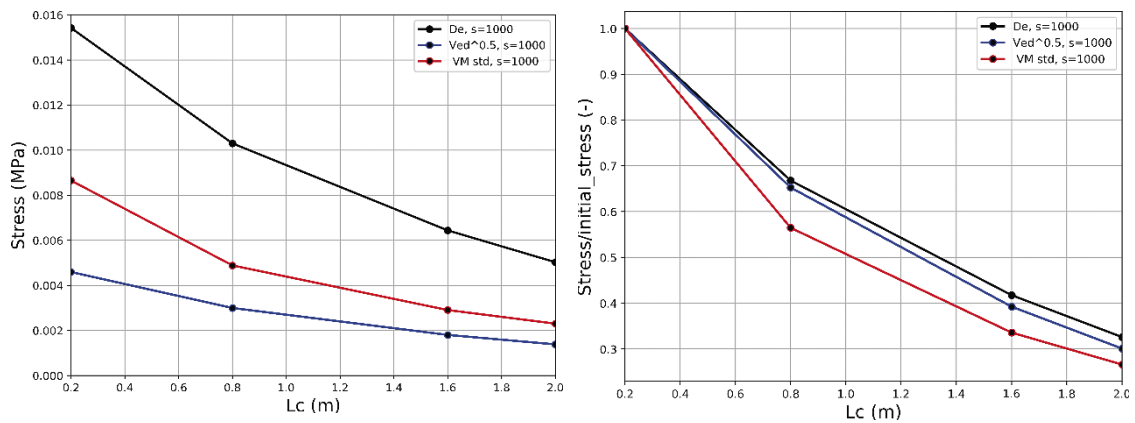


Figure 7-13. Evolution of the stress variability indicators with L_c for one DFN realization and $l_{min} = 0.2$ m. (left) $sdev(\sigma_e^*)$ (in red), D_e (in black) and $\sqrt{V_{elid}}$ (in blue). (right) Same convention and values normalized by the values at $L_c = 0.2$ m.

7.3.5 Focus on large fractures

The analyses relative to L_c are pursued to evaluate the change of average shear displacement for the few largest and explicit fractures in the tested DFN specimen.

Figure 7-14 qualitatively shows the distribution of displacements (arrows on the fracture plane) on one of the selected large fractures. The shear displacement orientation and maximum displacement amplitude is quite similar in both cases. The maximum magnitude is though higher for the model with more fractures (7.4×10^{-4} mm versus 6.4×10^{-4} mm).

Figure 7-15 and Figure 7-16 represent the evolution of shear displacement with L_c over the few selected largest fractures (the ones with a diameter > 2 m), for two DFN realizations. Displacements are normalized by the value at the initial tested L_c , on the right-side figures.

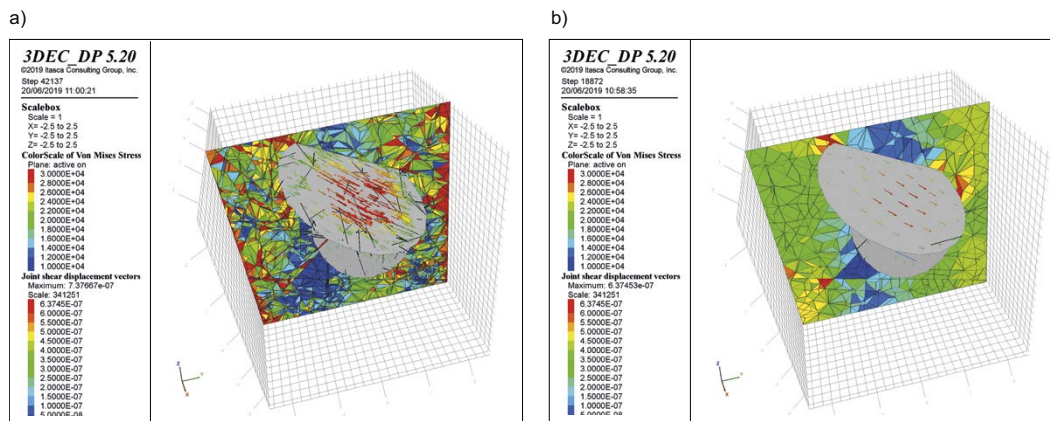


Figure 7-14. Shear displacement versus L_c on the largest fracture plane of a DFN realization, with a) $L_c = 0.4$ m and b) $L_c = 2$ m. The apparent increased concentration of displacement vectors observed in a) relatively to b) is simply due to finer mesh in this region because of intersections with other fractures.

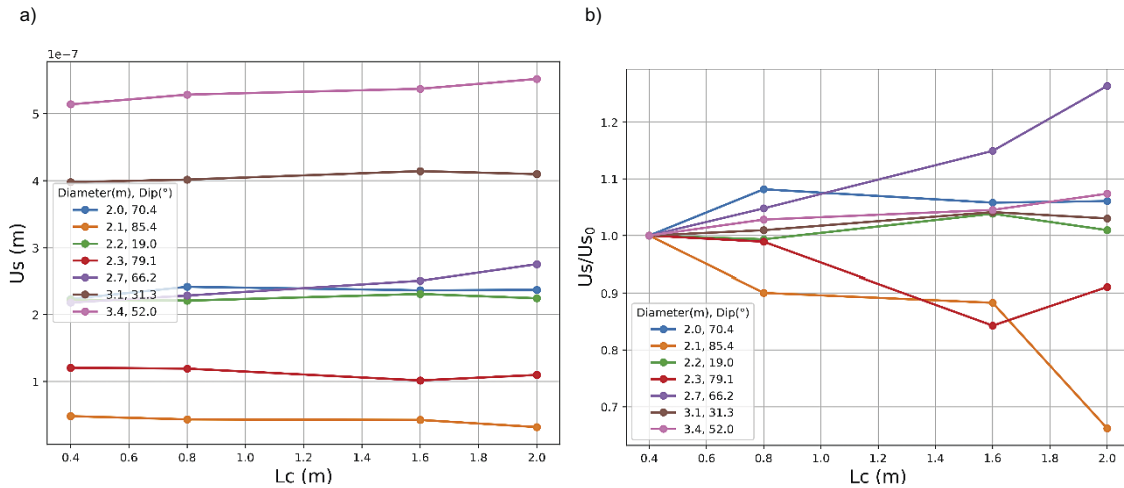


Figure 7-15. Evolution with L_c of the shear displacement on the largest fractures (7 selected fractures whose size and diameter are recalled in the legend) of the model (a) and shear displacements normalized by the initial value at $L_c = 0.4$ (b). Case $l_{min} = 0.4$ and seed $s = 1000$.

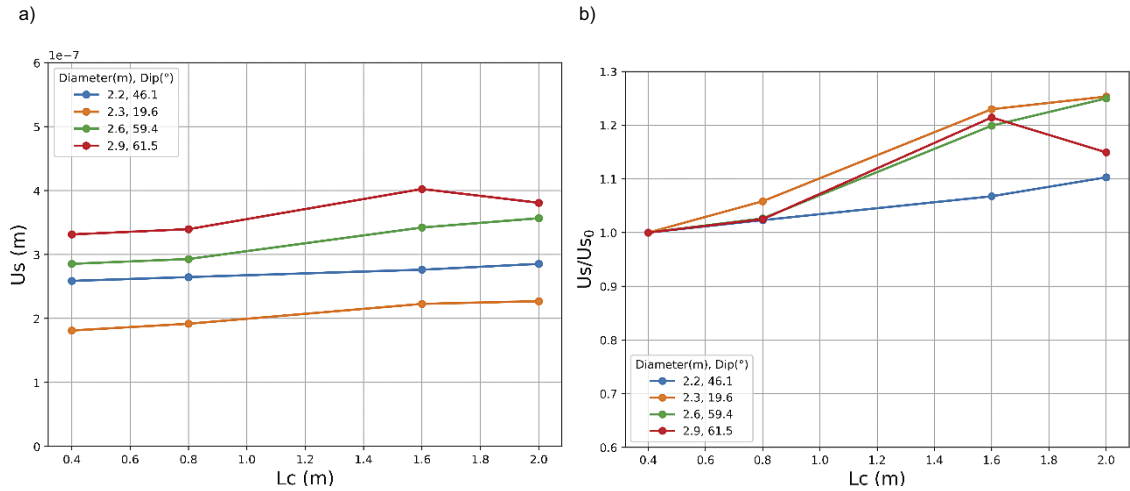


Figure 7-16. Evolution with L_c of the shear displacement on the largest fractures of the model (a) and shear displacement normalized by the initial value at $L_c = 0.4$ (b). Case $l_{min} = 0.4$ and seed $s = 3000$.

We observe a general tendency for the shear displacement of large fractures to increase when fewer fractures remain in the model (i.e., with increasing L_c). This is consistent with the previous observation (in Section 6.3.3) that the global effective stiffness is lower than the real effective stiffness measured locally around an explicit fracture. When replacing the surrounding of the fracture by an effective continuum medium with lower stiffness than the initial local stiffness, the consequence is an increase of the fracture displacement.

However, this observation is not true for all fractures. For the first DFN realization (Figure 7-14), some of the fractures have a lower shear displacement with increasing L_c . This could be explained by the position of these fractures relative to other fractures initially in the model (at low values of L_c). Consider, for instance, the case of a large fracture that crosses the stress concentration area located around the tip of a neighbor fracture. When the neighbor fracture is removed (with increasing L_c), the large fracture will be subject to lower stresses. If this effect is dominant by comparison to the decrease of the local surrounding rock stiffness, the fracture will witness a decrease of its shear displacement. In addition, the orientation of the fractures may be of importance too, acknowledging the shear potential on a fracture is not only relative to the fracture size but is just as much sensitive to the orientation of the fracture (and relatively to the stress field).

In total, the variation of shear displacement, between the model with all fractures ($L_c = l_{min}$) and the model with few fractures ($L_c = 2 m$), is less than 30 %.

7.3.6 Summary and recommendation

The analyses of stress fluctuations due to a change of L_c presented here are preliminary and will be further developed in the future. It is planned to *i*) systematically evaluate the stress variations scale dependency in the SRM specimen (i.e., not only at the zone size scale; *ii*) to pursue the identification of the fractures which are (due to their size, orientation and mechanical parameters) the most likely critical for given stress conditions, as a further step to optimize the limit between effective and explicit representation for mechanical simulations; and *iii*) to develop analytical relations between stress fluctuations and initial parameters of the SRM specimen (DFN and rock properties) and to predict the proportion of critical zones and their locations, as an introductory step toward strength modelling.

7.4 Test cases application

The approach has been applied recently to the FFM01 unit (Darcel et al. 2018) and to the Singö fault (Åkerlind 2019). The application to the FFM01 unit is summarized below. In this application, the purpose is to replace all the rock mass model (discrete fractures plus intact rock) by one effective medium (i.e. no discrete/explicit fracture is kept in the final model). For doing this, it is important to first evaluate the potential anisotropy and scale dependency of the effective elastic coefficients.

7.4.1 FFM01 Fracture Domain at Forsmark

In the following we summarize the parameters and results formerly presented by Darcel et al. (2018) for the rock mass in the FFM01 fracture domain at the Forsmark site. The data collected in the unit, located at a depth from 200 to 400 m, have led to definition of a DFN model (Glamheden et al. 2007; Follin 2008; SKB 2010) with 5 orientation sets (Figure 7-17a), 4 vertical and 1 sub-horizontal. The anisotropy resulting from these orientation sets is directly expressed in the stereonet plot in Figure 7-17b.

The fracture size density distribution model is based on the typical double power-law size distribution of the UFM approach (Davy et al. 2010). The transition scale l_c , between the two power-law regimes (the “growth” regime below l_c – subscript g , and the “ufm” regime above l_c – subscript u) is equal to 3.3 m. The fracture size density distribution model, $n(l)$, which defines the number of fractures by unit of volume, whose size is in the range ($l; l + dl$) is equal to:

$$n(l < l_c) = \alpha_g l^{-a_g} \quad (7-1)$$

$$n(l > l_c) = \alpha_u l^{-a_u} \quad (7-2)$$

With α_g and α_u the density terms – and a_g and a_u the scaling exponents- of the *growth* and *ufm* regimes, respectively. For the DFN model calibrated to the FFM01 unit, it comes that $\alpha_g = 1.23$ and $\alpha_u = 4.0$ the density terms – and $a_g = 3.0$ and $a_u = 4.0$. The FFM01 fracture size density distribution model is plotted in a log-log diagram in Figure 7-18.

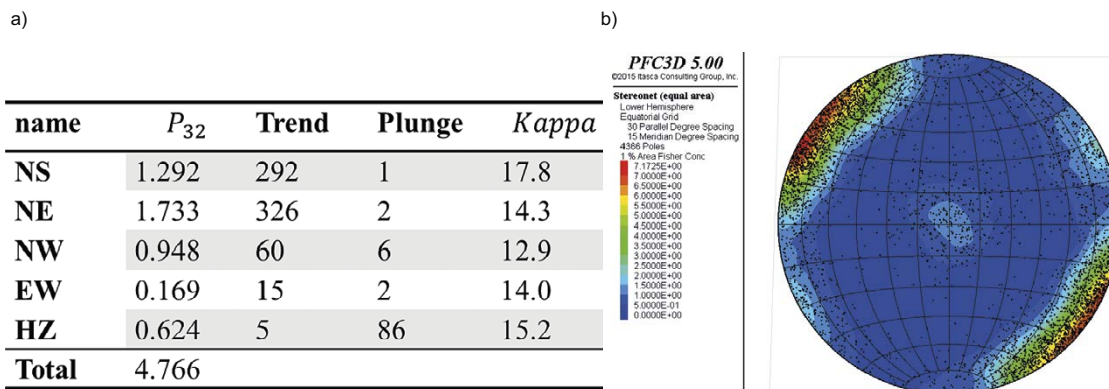


Figure 7-17. a) List of the orientation sets for the FFM01 unit, estimated from core log data. P_{32} is the fracture density estimated from core log data. Each orientation set is defined by a Fisher distribution model, with a mean orientation (trend and plunge) and dispersion κ . b) Stereonet of a DFN realization defined from the 5 orientation sets.

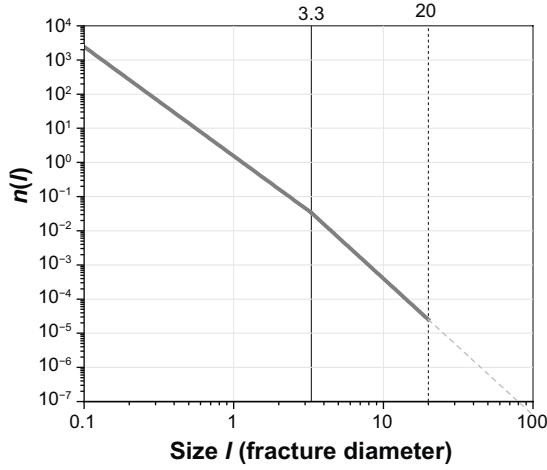


Figure 7-18. Fracture size density distribution model for the FFM01 unit.

The mechanical properties of the intact rock and of the fractures are the following. The intact rock is elastic and isotropic with a Young's modulus $E_m = 76 \text{ GPa}$ and Poisson's ratio $\nu_m = 0.25$. The fracture mechanical model is adapted from the Coulomb slip model with a constant cohesion equal to 1 GPa and friction angle $\phi = 37^\circ$, and a dependence of the fracture normal and shear stiffnesses, $k_n(\sigma_n)$ and $k_s(\sigma_n)$, on the normal stress acting on each fracture:

$$k_s(\sigma_n) = 46.55 \times \sigma_n^{0.4039} \times 10^6 \quad (7-3)$$

$$k_n(\sigma_n) = 2.28 \times \sigma_n^{0.822} \times 10^6 \quad (7-4)$$

Finally, the stress state applied at the FFM01 unit presents a minor principal stress that is vertical and a major horizontal principal stress with a trend equal to 145° (see values in Table 7-3).

Table 7-3. Remote stress field at 200 m depth.

σ_H (MPa)	σ_H trend ($^\circ$)	σ_h (MPa)	σ_v (MPa)
23.9	145	13.6	5.3

The workflow to make the prediction of the effective elastic properties is:

- generate several realizations of the DFN model, over given volume dimensions,
- for each fracture – assuming that the normal and shear stresses acting on the fractures are on average equal to the projection of the remote stress field (Table 7-3) – compute the stress related normal and shear stiffnesses, displacement and consecutive strain to the limit of the rock mass volume,
- derive the total strain from the sum of the contribution of each individual fracture, and
- derive the compliance tensor components.

The workflow is applied for the DFN model defined from a minimum fracture size of 0.1 m and for rock mass volumes of edge length L from 0.5 to 20 m. For each value of L , the fracture size distribution is truncated to L , so that no fracture larger than the evaluated domain is considered.

The resulting compliance tensor displays orthotropic properties (Darcel et al. 2018). The evolutions of the effective elastic components E_{xx} , E_{yy} , E_{zz} , G_{xy} , G_{yz} and G_{zx} with L are plotted in Figure 7-19.

Due to the nature of the DFN model fracture size density distribution, we note a scale effect with the decrease of the E_{ii} and G_{ij} components with increasing scale L . The extent of this effect results from the combination of the DFN geometrical properties (sizes), the fracture stiffnesses (k_s , k_n) and mechanical length $l_m = E_m/k_s$. The respective impact of the displacements due to the normal and shear stiffness components (Darcel et al. 2018) is such that, in the present conditions, the alteration of effective properties is mostly due to the shear displacement component. At the extreme, if k_s is negligible

(frictionless fractures, see Section 4.1), one would expect an endless scale effect (dashed lines in the figure). With the more realistic value of k_s , the scale effect vanishes roughly above 10 meters both for the Young's E_{ii} and shear G_{ij} components. At that scale, the anisotropy is such that the vertical modulus is decreased by about 12 % when compared to the intact rock, whereas is decreased by about 25 % for the horizontal modulus.

This test case shows that both scale and anisotropy effects are fully evaluated with the method. Moreover, testing a wider range of hypotheses, i.e. doing more sensitivity studies (over the parameters themselves and over more realizations), allows a quantitative assessment of the uncertainties over the parameters and of the variability due to the stochastic nature of the DFN modelling.

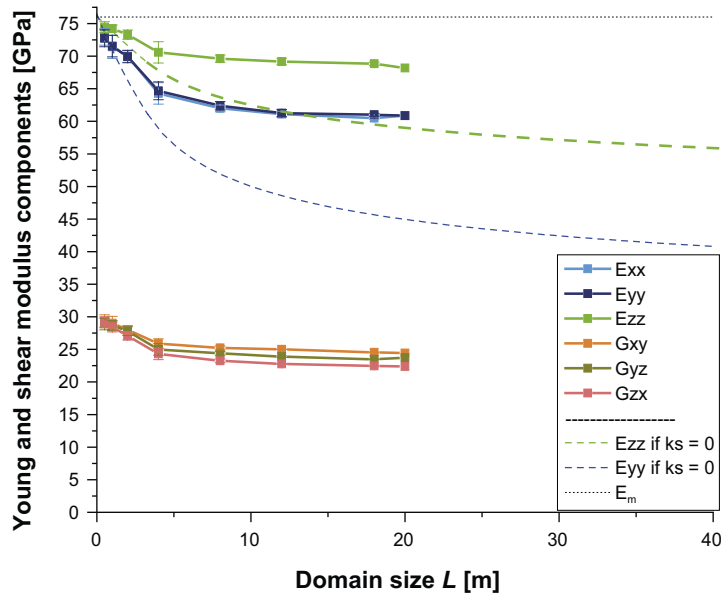


Figure 7-19. Evolution, with domain scale size, of the apparent effective elastic components E_{xx} , E_{yy} , E_{zz} , G_{xy} , G_{yz} and G_{zx} for realistic values of k_s (curves with filled symbols) and for frictionless fractures ($k_s \equiv 0$, dashed line).

8 Conclusions

The objective of this project was to develop a quantitative and sound methodology to assess effective elastic properties of fractured rock mass based on a Discrete Fracture Network (DFN) modelling approach for characterizing the rock mass (Selroos et al. 2021). The presented work covers all the developments carried out as part of the project, some of which are published in Darcel et al. (2018) and Davy et al. (2018).

The first step is the derivation of the relationships between the rock mass deformability (effective elastic properties with compliance tensor \bar{C}) and the geometrical properties of fracture networks, associated with their local fracture scale mechanical properties. The development is an extension of the well-known elastic solutions for free-slipping and disc-shaped cracks, with the addition of a frictional term (in-plane fracture resistance and shear stiffness property k_s , which defines the shear displacement below the frictional limit with a Coulomb law and free-slipping above this limit) and where both shear (k_s and friction envelop) and normal (normal stiffness k_n) displacements in the fracture plane are defined. We show that the fracture shear displacement is controlled by a combination of the fracture in-plane resistance and by the rock matrix resistance around the fracture, which is itself inversely proportional to the fracture size. We accordingly define a characteristic fracture size l_s (the stiffness length), below which deformation is dominated by the rock matrix resistance around the fractures and above which it is controlled by the resistance on the fracture plane. We emphasize that remote stress conditions necessary to trigger a slipping regime at a fracture embedded in the rock matrix must account for the stress partitioning at the fracture scale, between resistances of fracture in-plane and rock matrix at the fracture tips. Therefore, the remote stress value necessary to trigger the slipping regime in a fracture is larger than the fracture local Coulomb limit by a factor $\frac{k_s+k_m}{k_s}$, where k_m is the matrix-fracture stiffness (Equation (4-10)).

With the relationship established between a single fracture, the rock mass deformability and remote stress conditions, the next step is to sum up the contribution of all the individual fractures of a DFN to the rock mass deformation and to deduce the effective elastic components. Effective theory arguments are applied to account for fracture interactions when density of fractures in the DFN is large. All the derived relationships are confirmed by numerical simulations.

Next, these relationships are used to identify which of the DFN parameters (density, size distribution, etc) or mechanical parameters (elastic properties of the matrix, normal and shear stiffnesses of fractures) controls the effective elastic properties of the rock mass.

For some reference cases, simplified relationships have been established that link the DFN model properties (DFN P_{32} , percolation parameter p , fracture size range) and the effective elastic properties. If the fractures of a DFN are such that $k_s \gg k_m$, the effective elastic modulus is controlled by the DFN volumetric total surface of fracture (dependency proportional to the sum of fracture surfaces, in l^2). However, if fractures are such that $k_s \ll k_m$ then the effective elastic modulus is controlled by the DFN percolation parameter (dependency proportional to the sum of fracture “volumes”, in l^3). The latter occurs when fracture sizes are sufficiently smaller than l_s (the characteristic stiffness size). This causes a scale effect for the effective elastic properties.

The established relationships can be applied to derive the effective compliance tensor resulting from any DFN realization. This is exemplified with an application to one Fracture Domain (FFM01) of the Forsmark site. In this example, the rock mass model consists of an isotropic intact rock, a DFN model based on 5 fracture sets with a double power-law size distribution (UFM model) and normal and shear stiffnesses constitutive models based on a power-law relationship with the fracture normal stress.

In complement, several analyses are performed to evaluate the local stress fluctuations around the fractures within the rock mass specimen. They are all based on numerical simulations. The implemented stress fluctuation indicators aim at characterizing the variations around the mean stresses, without neglecting the tensorial aspect of stresses, and at potentially identifying scale effects. A first set of analyses is used as a support to the effective theory applied to account for the stress fluctuations that arise from the fracture interactions.

Finally, an exploratory study aims to analyse the consequences of gradually replacing part of the DFN with effective properties. Even if the average rock mass properties are well preserved by this methodology, this entails a reduction of the stress fluctuations. This is quantified over a few simulations. This study is ongoing, with the purpose to establish the relationship between the rock mass (and DFN) and stress conditions and the resulting distribution of stress fluctuations.

To conclude, the developed method shows for now its capacity to assess rock mass effective elastic properties, including a versatile description of the initial rock mass conditions and its capacity to characterize scale and anisotropic scale effects.

Additional exploratory studies show how it can be further developed to:

- assess the extent of stress fluctuations (in addition to effective average values),
- optimize the effective/discrete representation of the DFN for modelling application,
- develop the relationship between DFN and rock mass strength,
- prediction of critically stressed fractures and consequences on strength prediction,
- complete the method to account for refined fracture mechanical model (e.g. dilation term for critically stressed fractures) and to define the fracture mechanical opening, as a prerequisite to introduce the hydro-mechanical coupling between mechanical and hydraulic aperture at the fracture scale.

References

SKB's (Svensk Kärnbränslehantering AB) publications can be found at www.skb.com/publications.

- Andersson J, Christiansson R, Hudson J, 2002.** Site investigations strategy for Rock Mechanics Site Descriptive Model. SKB TR-02-01, Svensk Kärnbränslehantering AB.
- Barker J A, 2018.** Intersection statistics and percolation criteria for fractures of mixed shapes and sizes. *Computers & Geosciences* 112, 47–53.
- Barton N, Lien R, Lunde J, 1974.** Engineering classification of rock masses for the design of tunnel support. *Rock Mechanics* 6, 189–236.
- Bieniawski Z, 1973.** Engineering classification of jointed rock masses. *Civil Engineer in South Africa* 15. doi:10.1016/0148-9062(74)90924-3
- Bour O, Davy P, 1998.** On the connectivity of three-dimensional fault networks. *Water Resources Research* 34, 2611–2622.
- Bruner W M, 1976.** Comment on ‘Seismic velocities in dry and saturated cracked solids’ by Richard J. O’Connell and Bernard Budiansky. *Journal of Geophysical Research* 81, 2573–2576.
- Darcel C, Davy P, Le Goc R, Mas Ivars D, 2018.** Rock mass effective properties from a DFN approach. In *Proceedings of 2nd International Discrete Fracture Network Engineering Conference*, Seattle, 20–22 June 2018. American Rock Mechanics Association.
- Davy P, Darcel C, Le Goc R, Mas Ivars D, 2018.** Elastic properties of fractured rock masses with frictional properties and power-law fracture size distributions. *Journal of Geophysical Research: Solid Earth* 123, 6521–6539.
- Davy P, Le Goc R, Darcel C, Bour O, de Dreuzy J-R, Munier R, 2010.** A likely universal model of fracture scaling and its consequence for crustal hydro-mechanics. *Journal of Geophysical Research: Solid Earth* 115, 1978–2012.
- de Dreuzy J-R, Davy P, Bour O, 2000.** Percolation parameter and percolation-threshold estimates for three-dimensional random ellipses with widely scattered distributions of eccentricity and size. *Physical Review E* 62, 5948–5952.
- Deere D, 1963.** Technical description of rock cores. *Geologie und Bauwesen* 28.
- Deere D, 1968.** Geological considerations. In Stagg K G, Zienkiewicz O C (eds). *Rock mechanics in engineering practice*. London: Wiley, 1–20.
- Fabrikant V I, 1999.** Two arbitrarily located normal forces and a penny-shaped crack: a complete solution. *Mathematical Methods in the Applied Sciences* 22, 1201–1220.
- Follin S, 2008.** Bedrock hydrogeology Forsmark. Site descriptive modelling, SDM-Site Forsmark. SKB R-08-95, Svensk Kärnbränslehantering AB.
- Gao K, Harrison J P, 2016a.** Mean and dispersion of stress tensors using Euclidean and Riemannian approaches. *International Journal of Rock Mechanics and Mining Sciences* 85, 165–173.
- Gao K, Harrison J P, 2016b.** Characterising stress dispersion for stress variability analysis. In *Proceedings of ISRM International Symposium on In-Situ Rock Stress*, Tampere, Finland, May 2016. International Society for Rock Mechanics and Rock Engineering. Paper ISRM-ISRS-2016-016.
- Gao K, Harrison J P, 2017.** Generation of random stress tensors. *International Journal of Rock Mechanics and Mining Sciences* 94, 18–26.
- Gao K, Harrison J P, 2018a.** Multivariate distribution model for stress variability characterisation. *International Journal of Rock Mechanics and Mining Sciences* 102, 144–154.
- Gao K, Harrison J P, 2018b.** Scalar-valued measures of stress dispersion. *International Journal of Rock Mechanics and Mining Sciences* 106, 234–242.

- Glamheden R, Fredriksson A, Röshoff K, Kalsson J, Hakami H, Christiansson R, 2007.** Rock mechanics Forsmark. Site descriptive modelling Forsmark stage 2.2. SKB R-07-31, Svensk Kärnbränslehantering AB.
- Guéguen Y, Kachanov M, 2012.** Effective elastic properties of cracked rock – an overview. In Leroy Y M, Lehner F K (eds). *Mechanics of crustal rocks*. Vienna: Springer. (CISM Courses and Lectures 533), 73–125.
- Hakami E, Mas Ivars D, Darcel C, 2021.** Methodology for rock mechanics modelling of the Forsmark site. SKB R-20-13, Svensk Kärnbränslehantering AB.
- Hashin Z, 1988.** The differential scheme and its application to cracked materials. *Journal of the Mechanics and Physics of Solids* 36, 719–734.
- Hoek E, Brown E T, 1997.** Practical estimates of rock mass strength. *International Journal of Rock Mechanics and Mining Sciences* 34, 1165–1186.
- Hoek E, Brown E T, 2019.** The Hoek–Brown failure criterion and GSI – 2018 edition. *Journal of Rock Mechanics Geotechnical Engineering* 11, 445–463.
- Hoek E, Carter T G, Diederichs M S, 2013.** Quantification of the geological strength index chart. Proceedings of 47th US Rock Mechanics/Geomechanics Symposium, San Francisco, CA, 23–26 June 2013. American Rock Mechanics Association. ARMA 13-672.
- Itasca, 2016.** 3DEC – Three-Dimensional Distinct Element Code, version 5.2. Minneapolis, MN: Itasca.
- Jaeger J C, Cook N G W, Zimmerman R W, 2007.** Fundamentals of rock mechanics. 4th ed. Wiley.
- Kachanov M, 1987.** Elastic solids with many cracks: a simple method of analysis. *International Journal of Solids and Structures* 23, 23–43.
- Kachanov M, 1993.** Elastic solids with many cracks and related problems. In Hutchinson J W, Wu T Y (eds). *Advances in applied mechanics*. Vol 30. New York: Academic Press, 259–445.
- Kachanov M, Sevostianov I (eds), 2013.** Effective properties of heterogeneous materials. Dordrecht: Springer.
- Mas Ivars D, Pierce M E, Darcel C, Reyes-Montes J, Potyondy D O, Young R P, Cundall P A, 2011.** The synthetic rock mass approach for jointed rock mass modelling. *International Journal of Rock Mechanics and Mining Sciences* 48, 219–244.
- Mas Ivars D, Lope Álvarez D, Sánchez Juncal A, Ghazal R, Damjanac B, 2015.** Parametrisation of fractures – Estimation of fracture shear displacement due to excavation of new slots at the TASQ tunnel via numerical modeling. Posiva Working Report 2015-28, Posiva Oy, Finland.
- O’Connell R J, Budiansky B, 1974.** Seismic velocities in dry and saturated cracked solids. *Journal of Geophysical Research* 79, 5412–5426.
- Oda M, 1988.** An experimental study of the elasticity of mylonite rock with random cracks. *International Journal of Rock Mechanics and Mining Sciences & Geomechanics Abstracts* 25, 59–69.
- Oda M, Yamabe T, Ishizuka Y, Kumasaka H, Tada H, Kimura K, 1993.** Elastic stress and strain in jointed rock masses by means of crack tensor analysis. *Rock Mechanics and Rock Engineering* 26, 89–112.
- Pells P J, Bieniawski Z T, Hencher S R, Pells S E, 2017.** Rock quality designation (RQD): time to rest in peace. *Canadian Geotechnical Journal* 54, 825–834.
- Selroos J-O, Mas Ivars D, Munier R, Hartley L, Libby S, Darcel C, Davy P, Trincherro P, 2021.** Methodology for discrete fracture network modelling of the Forsmark site. Volume I: Concepts, data and interpretation methods. SKB R-20-11, Svensk Kärnbränslehantering AB.
- SKB, 2010.** Data report for the safety assessment SR-site. SKB TR-10-52, Svensk Kärnbränslehantering AB.
- Sneddon I N, Lowengrub M, 1969.** Crack problems in the classical theory of elasticity. New York: Wiley.

Staub I, Fredriksson A, Outters N, 2002. Strategy for a Rock Mechanics Site Descriptive Model. Development and testing of the theoretical approach. SKB R-02-02, Svensk Kärnbränslehantering AB.

Tchalenko J S, 1970. Similarities between shear zones of different magnitudes. Geological Society of America Bulletin 81, 1625–1640.

Åkerlind A, 2019. Elastic properties of the Singö zone from a discrete approach. Independent thesis, Advanced level. KTH, Stockholm, Sweden.

Rock mass classification systems

The way the fractures of the rock are considered to derive the rock mass properties has evolved significantly since the first rock mass quality index, the Rock Mass Quality Designation (RQD) introduced by Deere (1963), which preceded the Q system (Barton et al. 1974), the RMR (Bieniawski 1973) and the GSI with the associated Hoek-Brown constitutive model for rock mass strength envelope (Hoek and Brown 1997, 2019, Hoek et al. 2013). Their definitions are recalled below.

The Rock Quality Designation (RQD) was introduced in the mid-1960s (Deere 1968). It is a direct and empirical estimate of the rock quality, directly deduced from borehole core sections, as the percentage of core pieces whose length is larger than 10 cm:

$$RQD = \frac{\sum(\text{core pieces} > 10 \text{ cm})}{\text{core length}} * 100(\%) \quad (\text{A-1})$$

The classification ranks the rock quality from very poor (0 to 25 %) to excellent (90 to 100 %). The use of *RQD* to characterize the rock mass is now seriously criticized (Pells et al. 2017). Its extreme simplicity makes it very easy to use but it also severely limits the possibility to use it as an input for defining the rock mass elastic and strength properties. Estimating the *RQD* does not require a DFN model nor DFN assumptions. But it can be univocally related to the core fracture frequency P_{10} (which is a property broadly used in DFN models to quantify the density of fractures).

The Tunneling Quality Index, *Q* system, introduced by Barton et al. (1974), is based on several elements, amongst which the *RQD*:

$$Q = \frac{RQD}{J_n} \cdot \frac{J_r}{J_a} \cdot \frac{J_w}{SRF} \quad (\text{A-2})$$

in addition to the number of joint sets (J_n), the roughness of the most unfavorable joint or discontinuity (J_r), the degree of alteration or filling along the weakest joint (J_a), the water inflow (J_w), the stress condition given as the stress reduction factor (*SRF*).

The *RQD* also is a component of the Rock Mass Rating (*RMR*) System developed by Bieniawski (1973). The *RMR* gives a qualitative index of rock quality, from very poor to very good and index between 0 and 100. It is based on criteria similar to the *Q* system. The following six parameters are used to classify a rock mass using the *RMR* system: Uniaxial compressive strength of rock material, Rock Quality Designation (*RQD*), spacing of discontinuities, condition of discontinuities, groundwater conditions and orientation of discontinuities.

The *GSI*, introduced by Hoek in 1995, is a dimensionless number (between 5 and 85) which results from a qualitative assessment of the rock level of blockiness and the fracture surface conditions (Figure A-1).







<p>GEOLOGICAL STRENGTH INDEX FOR JOINTED ROCKS (Hoek and Marinos, 2000)</p> <p>From the lithology, structure and surface conditions of the discontinuities, estimate the average value of GSI. Do not try to be too precise. Quoting a range from 33 to 37 is more realistic than stating that GSI = 35. Note that the table does not apply to structurally controlled failures. Where weak planar structural planes are present in an unfavourable orientation with respect to the excavation face, these will dominate the rock mass behaviour. The shear strength of surfaces in rocks that are prone to deterioration as a result of changes in moisture content will be reduced if water is present. When working with rocks in the fair to very poor categories, a shift to the right may be made for wet conditions. Water pressure is dealt with by effective stress analysis.</p>		SURFACE CONDITIONS				
		VERY GOOD Very rough, fresh unweathered surfaces	GOOD Rough, slightly weathered, iron stained surfaces	FAIR Smooth, moderately weathered and altered surfaces	POOR Slickensided, highly weathered surfaces with compact coatings or fillings or angular fragments	VERY POOR Slickensided, highly weathered surfaces with soft clay coatings or fillings
STRUCTURE		DECREASING SURFACE QUALITY →				
	INTACT OR MASSIVE - intact rock specimens or massive in situ rock with few widely spaced discontinuities	90			N/A	N/A
	BLOCKY - well interlocked undisturbed rock mass consisting of cubical blocks formed by three intersecting discontinuity sets	80	70			
	VERY BLOCKY- interlocked, partially disturbed mass with multi-faceted angular blocks formed by 4 or more joint sets		60	50		
	BLOCKY/DISTURBED/SEAMY - folded with angular blocks formed by many intersecting discontinuity sets. Persistence of bedding planes or schistosity			40	30	
	DISINTEGRATED - poorly interlocked, heavily broken rock mass with mixture of angular and rounded rock pieces				20	
	LAMINATED/SHEARED - Lack of blockiness due to close spacing of weak schistosity or shear planes	N/A	N/A			10

Figure A-1. GSI chart from Hoek and Brown (2019).

SKB is responsible for managing spent nuclear fuel and radioactive waste produced by the Swedish nuclear power plants such that man and the environment are protected in the near and distant future.

skb.se